Genetic validation of *Pf*FKBP35 as an antimalarial drug target

Basil T. Thommen[1,2], Jerzy M. Dziekan[3], Fiona Achcar[4,5], Seth Tjia[3], Armin Passecker[1,2], Katarzyna Buczak[2], Christin Gumpp[1,2], Alexander Schmidt[2], Matthias Rottmann[1,2], Christof Grüring[1,2], Matthias Marti[4,5], Zbynek Bozdech[3], Nicolas M. B. Brancucci[1,2]

[1]Department of Medical Parasitology and Infection Biology, Swiss Tropical and Public Health Institute, 4123 Allschwil, Switzerland.

[2]University of Basel, 4001 Basel, Switzerland.

[3]School of Biological Sciences, Nanyang Technological University, Singapore.

[4]Wellcome Center for Integrative Parasitology, Institute of Infection, Immunity and Inflammation, University of Glasgow, Glasgow, UK.

[5]Institute for Parasitology, VetSuisse and Medical Faculty, University of Zurich, Zurich, Switzerland.

Correspondence:
Nicolas M. B. Brancucci, nicolas.brancucci@swisstph.ch

Keywords: malaria, *Plasmodium falciparum*, ribosome homeostasis, FKBP35, FK506, CETSA, antimalarial drugs

Abstract

Plasmodium falciparum accounts for the majority of over 600’000 malaria-associated deaths annually. Parasites resistant to nearly all antimalarials have emerged and the need for drugs with alternative modes of action is thus undoubted. The FK506-binding protein *Pf*FKBP35 has gained attention as a promising drug target due to its high affinity to the macrolide compound FK506 (tacrolimus). Whilst there is considerable interest in targeting *Pf*FKBP35 with small molecules, a genetic validation of this factor as a drug target is missing and its function in parasite biology remains elusive. Here, we show that limiting *Pf*FKBP35 levels are lethal to *P. falciparum* and result in a delayed death-like phenotype that is characterized by defective ribosome homeostasis and stalled protein synthesis. Our data furthermore suggest that FK506, unlike the action of this drug in model organisms, exerts its anti-proliferative activity in a *Pf*FKBP35-independent manner and, using cellular thermal shift assays, we identify putative FK506-targets beyond *Pf*FKBP35. In addition to revealing first insights into the function of *Pf*FKBP35, our results show that FKBP-binding drugs can adopt non-canonical modes of action – with major implications for the development of FK506-derived molecules active against *Plasmodium* parasites and other eukaryotic pathogens.

1 Introduction

Despite considerable progress in recent years, malaria remains one of the major global health threats (1). The apicomplexan parasite *Plasmodium falciparum* is responsible for the vast majority of the over 600'000 malaria deaths in 2020. Most of this burden is carried by infants and children under the age of five in sub-Saharan Africa. Malaria deaths increased by 12% compared to 2019, which can at least in part be explained by the COVID-19 related suspension of malaria control and treatment measures (1). In addition, the emergence of parasites resistant to most antimalarials, including artemisinin-based combination therapies, endangers current and future disease elimination efforts and underscores the need for developing drugs with alternative modes of action (2).

FK506 (tacrolimus), a well-characterized immunosuppressant, shows considerable activity against asexual blood stage parasites (3). *P. falciparum* encodes a single FK506-binding protein (FKBP) dubbed *Pf*FKBP35 (PF3D7_1247400), which is considered to be a promising drug target (4, 5). FKBPs belong to the immunophilin family and are conserved throughout the eukaryotic kingdom (6, 7). In contrast to the malaria parasite, most other eukaryotes encode several FKBPs that, besides showing high affinity for the FK506 drug, exert peptidyl-prolyl isomerase (PPIase) activity. The PPIase moiety catalyzes cis-trans isomerization of proline residues – an event thought to be rate-limiting for the folding of many proteins (8). Independent of their PPIase activity, FKBPs act as chaperones to prevent protein aggregation under stress conditions (9, 10). Furthermore, some FKBP variants play a role in cellular signaling or gene regulation (11, 12). Human FKBP12 for instance is best-known for its ability to form a complex with the immunosuppressant drugs FK506 and rapamycin. These complexes inhibit the phosphatase activity of calcineurin and the kinase activity of mTOR (mechanistic target of rapamycin), respectively (13). Amongst many other effects, this inhibition results in decreased T-cell activation. Of note, the regulatory role of *Hs*FKBP12 depends on the presence of rapamycin or FK506. In absence of drugs, this immunophilin neither interacts with mTOR nor with calcineurin and does hence not affect activity of these key components of eukaryotic cells. Due to the conserved nature of FKBPs, rapamycin and FK506 have also gained attention as potential antimicrobial drugs (3, 7).

Similar to its homologs in model organisms, *Pf*FKBP35 harbors PPIase and chaperoning activity *in vitro* (5). Despite sharing key features with FKBPs of other eukaryotes, its role in *P. falciparum* remains elusive. *Pf*FKBP35 is believed to interact with heat shock proteins (HSPs) and co-immunoprecipitates with cytoskeletal factors of *P. falciparum* (14). While *Pf*FKBP35

is inhibiting the phosphatase activity of recombinant calcineurin in a FK506-independent manner (15-17), it does not co-localize with calcineurin *in vivo* (16). The protein is expressed throughout the 48-hour intra-erythrocytic development of *P. falciparum* and is found within the cytosol of ring stage parasites. In the older trophozoite and the replicating schizont stages, the protein was reported to also localize to the nucleus (16). While a transposon-based mutagenesis screen suggests that *Pf*FKBP35 is essential for intra-erythrocytic replication (18), neither its cellular function nor its essentiality was confirmed experimentally in live parasites. The unknown role in parasite biology notwithstanding, *Pf*FKBP35 is considered to be a viable drug target and, given the fact that *P. vivax* and *P. knowlesi* encode FKBP homologs that exhibit comparable PPIase activities (19, 20), future FKBP-targeted therapies may be effective across different *Plasmodium* species.

Crystal structures of *Pf*FKBP35 in complex with FK506 and rapamycin revealed high affinity interactions with the FK506-binding domain of the protein (15, 21, 22). Consistent with these observations, *in vitro* enzyme activity assays showed that FK506 inhibits the PPIase activity of recombinant *Pf*FKBP35 in a dose-dependent manner (5). Previous research aimed at exploiting structural differences between human and parasite-encoded FKBPs to circumvent the immunosuppressive activity of drug-bound *Hs*FKBP12 (23-26). These efforts include investigation of non-covalent FKBP inhibitors such as adamantyl derivatives, macrocycles, the small molecule D44 (23-25, 27, 28) and the synthetic ligand for FKBP (SLF) as well as derivatives thereof designed to covalently bind *Pf*FKBP35 (29). While D44 shows promising antimalarial activity, it fails to alter thermostability of the FK506-binding domains of *Pf*FKBP35 and *Hs*FKBP12 *in vitro* (29), suggesting that this compound does not directly interact with *Pf*FKBP35. Up until now, *Pf*FKBP35 has not been validated as a drug target using reverse genetics, and the link between *Pf*FKBP35-interacting drugs and their antimalarial activity remains elusive (3).

Here, we generated inducible *Pf*FKBP35 knock-out, knock-down as well as over-expression cell lines and demonstrate that *Pf*FKBP35 is essential for asexual replication of blood forms. We show that the knock-out of *Pf*FKBP35 results in reduced levels of ribosomal proteins and stalled protein synthesis. However, these effects are not reflected in the parasite transcriptome, indicating a vital role at the post-transcriptional level. While the mechanistic link between *Pf*FKBP35 and ribosome homeostasis remains elusive, our data underpins the potential of *Pf*FKBP35 as a drug target and, using cellular thermal shift assays (CETSA), we corroborate the high affinity binding of FK506 to *Pf*FKBP35. Importantly, however, our data does not

support scenarios in which FK506 inhibits the essential function of *Pf*FKBP35, suggesting that it exerts its antimalarial activity in a *Pf*FKBP35-independent manner, which has major implications for the development of future FK506-based antimalarials and/or *Pf*FKBP35-inhibiting drugs.

2 Results

2.1 *Pf*FKBP35 is essential for asexual replication

In a first step, using CRISPR/Cas9-mediated gene editing, we engineered a *P. falciparum* cell line allowing for a conditional knock-down of *Pf*FKBP35 using the DD/Shield system (30, 31) (Figs. 1A and S1A-B). Despite the efficient depletion of *Pf*FKBP35 under knock-down conditions, parasites did not show apparent growth defects (Figs. S1C-D). Immunofluorescence assays (IFA) showed that *Pf*FKBP35 localizes to distinct foci within the parasite nucleus (Fig. 1B).

Next, we generated a cell line allowing for the conditional knock-out of the endogenous coding sequence using a dimerizable Cre recombinase (DiCre)-based system (32). Specifically, we introduced two *loxP* sites – one within a synthetic intron (33) downstream of the start codon and one after the stop codon of the *fkbp35* coding region – and added a *green fluorescent protein* (*gfp*) sequence downstream of this expression cassette (Figs. 1C, S2A). As a result, these NF54/iKO-FKBP35 parasites express tag-free, wild-type (WT) *Pf*FKBP35 protein under control conditions (FKBP35$^{\mathbf{WT}}$). Upon DiCre activation, the *loxP* sites are recombined and the *fkbp35* locus is excised from the parasite genome (Figs. 1C, S2B). Under these knock-out conditions (FKBP35$^{\mathbf{KO}}$), parasites express cytosolic GFP under control of the endogenous *fkbp35* promoter. This setup allows monitoring knock-out efficiency at the single cell level and revealed that DiCre successfully deleted *fkbp35* in the vast majority of parasites (Fig. 1D).

In a first attempt, we induced the *fkbp35* knock-out in synchronous ring stage NF54/iKO-FKBP35 parasites at 0-6 hours post erythrocyte invasion (hpi), i.e. prior to the expected peak transcription of *fkbp35* (34). These FKBP35$^{\mathbf{KO}}$ parasites showed a delayed death-like phenotype. In the first generation (G1), parasites completed intra-erythrocytic development without noticeable effects (Fig. 1E) and entered the next generation (G2) with a multiplication rate similar to that of the FKBP35$^{\mathbf{WT}}$ control population (Fig. 1F). In G2, however, FKBP35$^{\mathbf{KO}}$ parasites arrested at the late trophozoite/early schizont stage (approximately 30-36 hpi) with many cells failing to enter DNA replication in the S-phase (Fig. 1E). To investigate this

phenomenon in more detail, we induced the *fkbp35* knock-out at three different time points during the IDC. Similar to DiCre activation at 0-6 hpi, knocking out *fkbp35* at 12-18 hpi resulted in parasite death at the trophozoite/schizont stage of the subsequent generation. However, when induced at 24-30 hpi or 34-40 hpi in G1, parasites did not only complete the current IDC but also successfully passed through G2 before they eventually arrested in G3 (Fig. 1G). Considering that low *Pf*FKBP35 levels are sufficient to maintain the essential function of the protein, as observed with the NF54/iKD-FKBP35 parasites (see Fig. S1C-D), it is conceivable that proteins expressed between 0 and 24hpi, i.e. prior to deleting *fkbp35* from the genome, allow parasites to enter G3.

The delayed death of FKBP35$^{\mathbf{KO}}$ is reminiscent of a phenotype observed in apicoplast-deficient parasites (35, 36). We therefore tested if *Pf*FKBP35 is involved in apicoplast biology, i.e. the synthesis and/or export of isoprenoid precursors, but did not find evidence for an association with this organelle (Fig. S2C). Furthermore, given the reported interaction of *Pf*FKBP35 with heat shock proteins (14, 16), we also tested the parasite`s response to heat stress, but could not detect altered heat-susceptibility between FKBP35$^{\mathbf{KO}}$ and FKBP35$^{\mathbf{WT}}$ cells (Fig. S2D).

2.2 *Pf*FKBP35 is crucial for ribosome homeostasis and protein synthesis

To further elucidate the function of *Pf*FKBP35, we induced the *fkbp35* knock-out in early ring stages (0-6 hpi) and compared the proteomes of FKBP35$^{\mathbf{KO}}$ and FKBP35$^{\mathbf{WT}}$ parasites at the schizont stage of G1 (36-42 hpi) and at the trophozoite stage of the following generation (G2, 24-30 hpi) using a quantitative proteomics approach.

2.2.1 The knock-out of *Pf*FKBP35 causes accumulation of pre-ribosome components in G1

Consistent with the efficient deletion of *fkbp35* on the genomic level, FKBP35$^{\mathbf{KO}}$ schizonts of G1 showed a 19-fold (18.9 +/-5.7 s.d.) reduction of FKBP35 and GFP levels were increased by 84-fold (83.7 +/-38.5 s.d.) when compared to the control population (Fig. 2A, Table S1). Besides *Pf*FKBP35 and GFP, 50 parasite proteins were significantly deregulated in FKBP35$^{\mathbf{KO}}$ schizonts and 34 of them found at elevated levels compared to the FKBP35$^{\mathbf{WT}}$ control conditions. A gene ontology analysis using PANTHER (37) indicated enrichment of the "*pre-ribosome*" (fold enrichment = 30.4, p-value = 1.46E-5, 4/34 proteins) and "*nucleolus*" (fold enrichment = 6.77, p-value = 8.85E-4, 5/34 proteins) terms among these factors. While the pre-ribosome is a large subunit precursor of mature ribosomes, the nucleolus represents the primary

site for the biogenesis of ribosomal subunits (38). In contrast to factors being more abundant in knock-out parasites, none of the 16 factors with lower abundance in FKBP35^{KO} cells were associated with ribosome-related processes (Table S1). Despite being phenotypically silent in G1, the accumulation of pre-ribosome and nucleolar components hints at perturbed ribosome maturation in these cells. Specifically, it is conceivable that the observed buildup of ribosome intermediates results from reduced anabolic activity, i.e. the stalling of nucleolar pre-ribosome assembly (39).

Notwithstanding these effects, FKBP35^{KO} cells were equally sensitive to the translation inhibitor cycloheximide compared to their FKBP35^{WT} counterparts (Fig. 2B), indicating that ribosome function is not compromised at this point in time (40). This is consistent with normal cell cycle progression in G1 and unaltered multiplication rates of FKBP35^{KO} parasites, as described above (see Figs. 1E-F), and shows that the prominent depletion of *Pf*FKBP35 does not have a major impact on parasite viability in G1.

2.2.2 *Pf*FKBP35 is essential for maintaining normal levels of functional ribosomes in G2

In the following generation (G2, 24-30 hpi), the proteome of FKBP35^{KO} trophozoites showed substantial differences. Despite the absence of morphological changes at this point in time, 216 proteins were significantly deregulated (Fig. 2C). Among these, 50 proteins were found at higher abundance compared to FKBP35^{WT} and their gene ontology terms point towards an effect on processes involved in energy metabolism (Fig. 2D).

The majority of deregulated factors (166 of 216) in G2, however, were less abundant in FKBP35^{KO} compared to the FKBP35^{WT} control cells. Very prominently, 20 of the top 50 hit molecules are ribosomal proteins that, on average, show a two-fold reduction (2.0 +/- 0.4 s.d.) in FKBP35^{KO} parasites (Table S1). It is therefore not surprising that PANTHER identified the knock-out of *Pf*FKBP35 to mainly affect ribosome-related processes, such as "*cytoplasmic translation*", "*ribosome assembly*", and "*ribosomal large subunit biogenesis*" (Fig. 2D) (37).

To assess if the reduced levels of ribosomal proteins result in lower protein synthesis rates, we employed the "surface sensing of translation" (SUnSET) technique. SUnSET is based on incorporation of the tyrosyl-tRNA analogue puromycin into nascent peptide chains and thereby allows monitoring newly synthesized proteins (41). As expected, we found that FKBP35^{KO} trophozoites in G2 (24-30 hpi) showed reduced translation rates compared to the FKBP35^{WT}

control population (Fig. 2E), while protein synthesis was not affected under control conditions (rapamycin-induced DiCre activation in the NF54/DiCre parental line (Fig. S2E)).

Taken together, these results indicate that, under knock-out conditions, *Pf*FKBP35 levels become limiting for ribosome maturation late during schizogony of G1, without having immediate effects on the steady-state levels of mature ribosomes. The knock-out of *Pf*FKBP35 is thus phenotypically silent in G1. In absence of a continuous supply of mature ribosomes under FKBP35^{KO} conditions, however, FKBP35^{KO} parasites fail at maintaining translation at a level that would support normal parasite development in the next generation (G2).

2.3 The knock-out of *Pf*FKBP35 is transcriptionally silent

To examine if the altered proteome of FKBP35^{KO} parasites is the result of *Pf*FKBP35-controlled transcription, we compared the transcriptional profiles of FKBP35^{WT} and FKBP35^{KO} in a time course RNA-Sequencing (RNA-Seq) experiment spanning two IDCs. Specifically, we induced the knock-out of FKBP35 in synchronous parasites at 0-6 hpi and collected RNA from parasite populations at three and four subsequent time points (TPs) in G1 and G2, respectively (Figs. 3A, S3A). With the exception of TP7, these time points cover a time frame during which FKBP35^{KO} cells cannot be distinguished from their FKBP35-expressing counterparts on a morphological level (compare Fig. 1E).

As expected, the transcriptome of FKBP35^{KO} showed a prominent reduction of steady-state *fkbp35* transcripts already in TP1 (11.3-fold +/-2.0 s.d.) compared to the FKBP35^{WT} control population (Fig. S3B, Table S2). During peak transcription at 30-36 hpi (TP2), this difference increased to 240-fold (238.4 +/-20.0 s.d.) and, consistent with the efficient recombination at the *fkbp35* locus, these cells started transcribing *gfp*. Notwithstanding the prominent depletion of *fkbp35* transcripts, the transcriptome of FKBP35^{KO} is only marginally affected up to and including 24-30 hpi in G2 (TP6). By contrast, at 30-36 hpi (TP7) the transcription of knock-out parasites shows major changes (Fig. 3B). Considering the appearance of morphological changes in FKBP35^{KO} at this time point, effects on the transcriptome are unlikely to represent specific activities of *Pf*FKBP35 in gene regulation. Indeed, mapping the transcriptome of individual time points to a high resolution reference (42), revealed a significant slow-down of FKBP35^{KO} compared to FKBP35^{WT} parasites at TP7 (Figs. 3C, S3C). This indicates aborted cell cycle progression in FKBP35^{KO} parasites during a phase that is characterized by a rapid increase in biomass – possibly due to a translation and/or size-dependent cell cycle checkpoint (43). At

earlier time points (TP1-TP6), the transcriptomes of FKBP35^{KO} and FKBP35^{WT} are highly comparable and the differences observed on the level of individual genes clearly fail at explaining the proteomic changes observed in FKBP35^{KO} parasites at 24-30 hpi in G2 (TP6), reiterating that the essential activity of *Pf*FKBP35 is linked to transcription-independent processes.

2.4 Probing FK506 interactions in Cellular Thermal Shift Assays (CETSA)

*Pf*FKBP35 emerged as a promising antimalarial drug target (4) and considerable efforts were made to define interactions of this immunophilin with small molecules in the last decade (24-26, 44). Several studies conclusively demonstrated that FK506 – the most well-known ligand of mammalian FKBPs (45) – binds to *Pf*FKBP35 (15, 21, 22) and kills asexual blood stage parasites with a half-maximal inhibitory concentration (IC50) in the low micromolar range at 1.9 µM (3).

To investigate interactions of FK506 with *P. falciparum* proteins, we used the *cellular thermal shift assay followed by mass spectrometry* (MS-CETSA). This approach exploits the fact that, once drug-protein complexes are formed, thermostability of the target protein is altered (46). We applied the so-called *isothermal dose-response* variant of CETSA using FK506 (47). Here, target proteins are identified based on their dose-dependent stabilization by drugs under thermal challenge (different temperatures) when compared to a non-denaturing condition (37 °C), using the change in the area under the curve (ΔAUC) and the dose-response curve goodness of fit (R^2) as metrics (Fig. 4A) (47).

2.4.1 CETSA identifies targets of FK506

In a first step, we performed CETSA in combination with drug-exposed protein extracts. Since proteins lose their physiological context during the process of protein extraction, this variant of the CETSA approach is designed to identify direct protein-drug interactions (46, 47). Not surprisingly, we found *Pf*FKBP35 to be stabilized by FK506 in a dose-dependent manner when challenged at 60 °C with a half maximal effective concentration (EC50) of 152.0 nM (Fig. 4B). The fact that FK506 exhibits its stabilizing activity already in the low nanomolar concentration range indicates high affinity interactions between the protein-drug pair.

Besides *Pf*FKBP35, FK506 stabilizes a number of other proteins in a dose-dependent manner (Figs. 4C and S6). A few of these factors show pronounced sigmoidal stabilization profiles and are predicted to be essential (Fig. 4C) (18). Amongst others, N6-methyl transferase MT-A70 (PF3D7_0729500), histone deacetylase HDA2 (PF3D7_1008000), pre-mRNA-splicing factor CEF1 (PF3D7_1033600), FeS cluster assembly protein SufD (PF3D7_1103400) and the H/ACA ribonucleoprotein complex subunit 1 (PF3D7_1309500) showed most pronounced stabilization profiles (Fig. S6 and Table S3). In contrast to *Pf*FKBP35, most of these likely essential candidates are stabilized at FK506 concentrations close to the drug`s IC50 (3). It can therefore not be excluded that the binding of FK506 to at least one of these factors is contributes to the antimalarial activity of the drug.

2.4.2 The *Pf*FKBP35/FK506 pair interferes with ribosomal complexes

Given the high-affinity interaction of *Pf*FKBP35 with FK506 and its association with ribosomal proteins, we set out to describe the native context of *Pf*FKBP35 using the "live cell variant" of CETSA. In contrast to focusing exclusively on direct protein-drug interactions, live cell CETSA allows capturing drug-induced shifts in protein stability beyond those of direct binding partners (47) and amongst others allows identifying factors present in the same protein complex as the target protein. To do so, CETSA takes advantage of the fact that factors within complexes have similar denaturation temperatures due to their co-aggregation upon heat-induced denaturation (48). As a consequence, this CETSA variant generally identifies more factors compared to the protein extract-based CETSA approach (Fig. 4A).

As expected, and confirming the results above, live cell CETSA shows that FK506 alters the thermal stability of *Pf*FKBP35 already at very low drug concentrations when challenged at 60 °C with an EC50 of 286.7 nM (Fig. 4B). Interestingly, and in contrast to the protein lysate-based approach, live cell CETSA revealed that more than 50 ribosomal proteins are stabilized in presence of FK506 when challenged at 55 °C, with a median EC50 of 45.9 nM (25th percentile = 34.2, 75th percentile = 58.9). Of note, these ribosomal proteins were stabilized at virtually identical FK506 concentrations (Figs. 4D, and S7), indicating that the drug – directly or indirectly – interacts with ribosomal complexes. This is in further agreement with the fact that these ribosomal factors were not identified by protein lysate-based CETSA (compare Figs. 4A, S6).

Worth mentioning, we observed a drug dose-dependent increase in soluble protein abundance of ribosomal proteins also under non-denaturing conditions, i.e. at 37 °C, with a median EC50

of 1.94 µM (25th percentile = 1.85, 75th percentile = 2.1) (Figs. 4D, S7). Generally, due to the absence of a denaturing heat challenge, such a drug-dependent enrichment in soluble protein levels does not indicate binding-induced thermal stabilization of proteins (47). Instead, this can be the result of increased protein synthesis, altered protein conformation or, alternatively, occur in response to factors disengaging from larger protein complexes. The fact that FK506 solubilizes a high number of ribosomal proteins within a very narrow concentration window also at 37 °C, implies that these factors are liberated from the same ribosomal complex or from complexes that interact with each other and shows that FK506 negatively affects stability of ribosomal structures in live cells. However, these effects are limited to high, presumably saturating FK506 concentrations. Importantly, the vast majority of ribosomal proteins identified in live cell CETSA are shared with those de-regulated in *Pf*FKBP35 knock out cells (Fig. 4E), pointing towards a shared localization of FK506 and its *Pf*FKBP35 target in live parasites.

Together with the above-described importance of *Pf*FKBP35 in ribosome homeostasis, these results strongly suggest that FK506 is recruited to the activity site of *Pf*FKBP35 – most probably the nucleolar maturation sites of ribosomes – where it interacts with ribosomal complexes.

2.1 FKBP-targeting drugs fail at inhibiting the essential function of *Pf*FKBP35

Considering the proposed direct interaction between FK506 and FKBP35 in *P. falciparum*, we expected that FKBP35^{KO} parasites show altered sensitivity to the drug. Consistent with published data, FK506 killed FKBP35^{WT} cells with an IC50 of 1942 nM (+/-193 nM s.d.) when administered at 4-10 hpi (Fig. 4F). Surprisingly however, and despite the prominent depletion of the protein under knock-out conditions, FKBP35^{KO} and FKBP35^{WT} parasites were equally sensitive to FK506 (IC50 = 1741 nM +/- 187 s.d.) (Fig. 4F). Similarly, neither the efficient knock-down of *Pf*FKBP35 in NF54/iKD-FKBP35 parasites (compare Fig. S1C), nor its over-expression (OE) in NF54/iOE-FKBP35 cells (Fig. S4A-C), resulted in the expected sensitivity change to FK506 treatment (Fig. 4G). In addition to this apparent independence of the drug to varying *Pf*FKBP35 levels, and in agreement with earlier studies (3, 24, 49), FK506 unfolds its antimalarial activity within the same cycle after treatment. Standing in stark contrast to the delayed death-like phenotype of FKBP35^{KO} parasites (compare Fig. 1E-G), this immediate activity on parasite survival substantiates the notion that FK506 must target essential parasite factors other than *Pf*FKBP35.

To rule out that the timing of drug exposure is masking expected links between FK506 and *Pf*FKBP35, we tested whether administering FK506 at 30-36 hpi and 36-42 hpi (instead of 4-10 hpi) affects parasite survival in a *Pf*FKBP35-dependent manner. However, we did not observe a change compared to FKBP35$^{\mathbf{WT}}$ parasites (Fig. S5A), ruling out the possibility that FKBP35$^{\mathbf{KO}}$ parasites were killed by FK506 before *Pf*FKBP35 levels were different in the two populations. Further, to account for a scenario in which the activity of FK506 on *Pf*FKBP35 is masked by a temporal delay between drug exposure and parasite killing, we induced the knock-out of *Pf*FKBP35 at 34-40 hpi (instead of 0-6 hpi) and allowed FKBP35$^{\mathbf{KO}}$ parasites to proceed to G2, before exposing them to different FK506 concentrations. Despite these efforts, FKBP35$^{\mathbf{WT}}$ and FKBP35$^{\mathbf{KO}}$ parasites were equally sensitive to FK506 (Fig. S5B, S5C) and the calcineurin inhibitor cyclosporin A (Fig. S5D-E).

In addition to FK506, we evaluated the *Pf*FKBP35-specific inhibitor D44 (N-(2-Ethylphenyl)-2-(3h-Imidazo[4,5-B]pyridin-2-Ylsulfanyl)acetamide) but, surprisingly, we failed to reproduce the previously reported dose-response effect (24). We tested D44 from two suppliers using NF54/iKO-FKBP35, NF54 wild type and K1 parasite strains using different assay setups, including the gold standard method that is based on the incorporation of tritium labeled hypoxanthine into DNA of replicating cells (50). Still, we could not detect any activity of D44 on asexual replication of blood stage parasites (Figs. S5F-G).

Taken together, these results are in clear conflict with the perception that FK506 and D44 target the essential activity of *Pf*FKBP35.

3 Discussion

Members of the FKBP family are involved in regulating diverse cellular processes in eukaryotic as well as in prokaryotic cells (8, 51). In contrast to most other eukaryotes, the human malaria parasite *P. falciparum* encodes a single FKBP only (16). The enzymatic activity of *Pf*FKBP35, as well as the interactions of the protein with FKBP-targeting drugs, was subject to considerable drug-focused research *in vitro*. Besides demonstrating the drug`s affinity to *Pf*FKBP35 by co-crystallization, these efforts uncovered that FK506 inhibits enzymatic activity of the protein`s PPIase domain (5). Together with the anti-malarial activity of FK506, these data offered compelling evidence for an essential but yet uncharacterized role of *Pf*FKBP35 during blood stage development of *P. falciparum*.

Here, we set out to investigate the role of *Pf*FKBP35 in parasite biology. Using an inducible knock-out approach, we show that *Pf*FKBP35 is indeed essential for intra-erythrocytic

development of asexually replicating *P. falciparum* parasites and CETSA experiments confirmed high affinity binding of FK506 to its *Pf*FKBP35 target. While the knock-out of *Pf*FKBP35 does not markedly affect transcription, FKBP35$^{\mathbf{KO}}$ cells show reduced levels of ribosomal proteins and impaired protein synthesis on the global scale. Surprisingly however, these effects, as well as the consequent death during the late trophozoite/early schizont stage, only manifest in the cycle following knock-out induction without affecting cell cycle progression in the first generation (G1) or multiplication rates from G1 to G2. In contrast to the delayed death-like phenotype of FKBP35$^{\mathbf{KO}}$ cells, FK506 unfolds its parasiticidal activity without a lag phase, i.e. within the IDC of treatment (24), and the dose-response relationship between FK506 and parasite death is irresponsive to altered *Pf*FKBP35 levels. Taken together, our data strongly indicate that the parasite-killing activity of FK506 is *Pf*FKBP35-independent.

Knocking out *Pf*FKBP35 early during intra-erythrocytic development has only minor effects on the parasite proteome in G1. Being relatively subtle, these changes may still point towards an important function of *Pf*FKBP35: Factors associated with the nucleolus – the site of ribosome biogenesis – are found at higher abundance in knock-out cells. In the next cycle, FKBP35$^{\mathbf{KO}}$ parasites show a dramatic decrease of factors associated with ribosome- and translation-related processes and, likely a consequence thereof, globally reduced protein synthesis during trophozoite development (G2, 24-30 hpi). Importantly, at this point in time, FKBP35$^{\mathbf{KO}}$ cells still show ordinary morphology and their transcriptional activity remains largely unaffected. The observed changes in the abundance of ribosomal factors must therefore result from transcription-independent activity of *Pf*FKBP35. While ribosomal components are present at higher levels in G1, they are drastically reduced in FKBP35$^{\mathbf{KO}}$ cells in G2. These opposing effects likely result from *Pf*FKBP35 activity in a shared cellular process. Specifically, it is conceivable that low *Pf*FKBP35 levels inhibit ribosome maturation in G1, explaining the accumulation of (pre-) ribosomal factors. While the levels of functional ribosomes are sufficient to support continued translation in G1, ribosomes likely become limiting in the next generation (G2), which eventually results in stalled translation activity and concomitant parasite death at the onset of schizogony.

In contrast to the significant effects on the protein levels in G2, the transcription of FKBP35$^{\mathbf{KO}}$ remains largely unaffected by the loss of *Pf*FKBP35 and becomes apparent only during late trophozoite/early schizont development in G2 (30-36 hpi); i.e. at a time during which cell cycle progression is slowed down in FKBP35$^{\mathbf{KO}}$ parasites. In fact, at this stage the transcriptional signature of FKBP35$^{\mathbf{KO}}$ parasites is dominated by the slowed progression through intra-

erythrocytic development, rather than resulting from specific gene regulatory events. While this stalling is consistent with the observed effects on ribosome homeostasis and protein synthesis, it demonstrates that, in contrast to certain FKBP family members in other organisms, *Pf*FKBP35 does not have apparent roles in transcriptional control.

Regarding the well-characterized and fast-acting parasiticidal activity of FK506 on *P. falciparum*, it was somewhat surprising to observe a delayed death-like phenotype for *Pf*FKBP35 knock-out parasites (24). We hence set out to investigate unifying explanations. The delayed death of FKBP35$^{\mathbf{KO}}$ parasites is most easily be explained by residual activity of *Pf*FKBP35 proteins synthesized prior to inducing the genomic knock-out of *fkbp35*. In such a scenario, low *Pf*FKBP35 in FKBP35$^{\mathbf{KO}}$ would be sufficient to allow completion of the IDC, before eventually dropping below a level that is required for supporting parasite survival in the next cycle. Despite intense efforts, we failed at confirming this hypothesis and our data strongly favors an alternative scenario in which FK506 kills parasites in a *Pf*FKBP35-idenpendent manner. Aside from the fact that FK506 exerts its parasiticidal activity within the same IDC, neither the conditional knock-out, knock-down nor the overexpression of *Pf*FKBP35 altered the parasite's sensitivity to FK506; and this irrespective of the profoundly deregulated *Pf*FKBP35 levels in the respective mutant lines (Fig. 4F). For instance, administering FK506 36 hours post induction of the knock-out in early ring stages (36-42 hpi) – i.e. at a time point where FKBP35$^{\mathbf{KO}}$ cells are only left with about 5% of the regular *Pf*FKBP35 levels (19-fold reduction compared to FKBP35$^{\mathbf{WT}}$ parasites, Fig. 2A) – does not affect the dose-response of parasites to the drug. Further, our attempts to demonstrate that the timing of drug exposure is masking the expected links between FK506 and its *Pf*FKBP35 drug target failed (compare Figs. 4A and S5A-C). Our data is thus incompatible with the notion that the parasite-killing activity of FK506 results from inhibiting the essential function of *Pf*FKBP35.

Since binding of FK506 to *Pf*FKBP35 alone cannot explain the drug's antimalarial activity, we aimed identifying additional FK506 targets. CETSA performed on protein lysates identified a number of parasite factors binding to FK506. Compared to the *Pf*FKBP35/FK506 pair, however, these interactions are of considerably lower affinity. The adenosine-methyltransferase MT-A70 (PF3D7_0729500) and the pre-mRNA-splicing factor CEF1 (PF3D7_1033600), for instance, were stabilized by FK506 with EC50 concentrations of 2.0 and 3.1 µM, respectively. While this affinity is relatively poor compared to the strong interaction formed between *Pf*FKBP35 and FK506, one should be cautious designating the binding of FK506 to these proteins as irrelevant "*off-target*" effects. In fact, their inhibition may hypothetically mask

effects of FK506 on *Pf*FKBP35 – a possibility that shall briefly be discussed in the following section.

Assuming that FK506 is inhibiting the essential function of *Pf*FKBP35, one would expect parasites to show a delayed death-like phenotype similar to that observed in FKBP35$^{\mathbf{KO}}$ parasites. The presence and inhibition of other essential targets may, however, mask such an effect. Consistent with this possibility, FK506 kills *P. falciparum* parasites at 1.9 µM (+/-0.2 µM s.d.), i.e. at concentrations similar to those required for stabilizing MT-A70 and CEF1 under thermal challenge in CETSA. However, numerous attempts to prove that FK506 indeed inhibits essential *Pf*FKBP35 functions failed: Neither knocking out *Pf*FKBP35 at different time points nor adding FK506 to different stages of FKBP35$^{\mathbf{KO}}$ parasites could provide evidence for a *Pf*FKBP35-dependent effect. This indicates that either the binding of FK506 does not interfere with the essential role of *Pf*FKBP35, or that *Pf*FKBP35 is inhibited only at high FK506 concentrations that also inhibit other essential factors. In this context it is worth mentioning that parasites remain unaffected by a highly efficient knock-down of endogenous *Pf*FKBP35 (observed with NF54/iKD-FKBP35; compare Figs. S1C-D), which demonstrates that very low protein levels are sufficient to maintain the essential function of *Pf*FKBP35. It is thus conceivable that high FK506 concentrations are required to fully inhibit *Pf*FKBP35 – a view that is further supported by data obtained with the live cell CETSA approach discussed hereafter.

Besides identifying direct binding of drugs to their target, live cell CETSA allows capturing indirect effects on factors that act in the same pathway or in the same protein complex as the drug-bound target (47). While this approach confirmed the high affinity binding of FK506 to *Pf*FKBP35, it also revealed that more than 50 ribosomal proteins share a very prominent CETSA signature: First, they are thermally stabilized by FK506 within a narrow concentration window of the drug. Second, higher levels of FK506 increase the solubility of these ribosomal components also at 37 °C. These results indicate that the FK506/*Pf*FKBP35 pair interacts with ribosomal complexes and that FK506 is able to induce the dissociation of these ribosomal structures under physiological conditions. Importantly, and in contrast to the binding of FK506 to *Pf*FKBP35, this effect on ribosomes is only observed at high concentrations of the drug. Together, these data likely explain the discrepancy observed between the high binding affinity of FK506 for *Pf*FKBP35 and the low or even absent effect of the drug on *Pf*FKBP35 function in blood stage parasites.

In line with our data, previous biochemical approaches revealed potential links between *Pf*FKBP35 and ribosomes. Using co-immunoprecipitation, Leneghan and colleagues revealed that *Pf*FKBP35 is interacting with 480 proteins, of which 31 are ribosomal factors (14). Indeed, FKBP family members are essentially involved in controlling ribosomes in other systems. The human FKBP variant *Hs*FKBP25, for instance, is recruited to the pre-ribosome where its chaperone activity appears to be required for the assembly of the ribosomal large subunit (52). While the FKBP variant of yeast, Fpr4, interacts with the ribosome biogenesis factor Nop53 (53), the *Escherichia coli* trigger factor (TF) is part of the ribosomal complex and crucial for the folding of nascent proteins (54, 55). Considering the marked reduction of ribosomal proteins in FKBP35$^{\mathbf{KO}}$ parasites, it is tempting to speculate that *Pf*FKBP35 is chaperoning ribosome biogenesis similar to Fpr4 and FKBP25 in *Saccharomyces cerevisiae* and *humans*, respectively.

The fact that *Pf*FKBP35 localizes to distinct nuclear foci and its depletion causes dysregulation of ribosomes points towards a role within the nucleolus – the nuclear compartment driving ribosome biogenesis (38). Using IFAs, we found that *Pf*FKBP35 does not co-localize with the nucleolar marker fibrillarin (56) (Fig. S8). However, its localization appears to be intertwined with that of this rRNA methyltransferase. Specifically, *Pf*FKBP35 is mostly found in close vicinity to fibrillarin-rich regions. Nucleoli in eukaryotic cells generally consist of two or, in higher eukaryotes, three sub-compartments. Of those, the granular component (GC) represents the site of pre-ribosome assembly and encompasses fibrillarin-enriched central regions of nucleoli (57). The spatial correlation observed between *Pf*FKBP35 and fibrillarin may thus indicate localization to different sub-nucleolar compartments, with *Pf*FKBP35 occupying the GC area of the nucleolus.

In summary, we demonstrate that limiting *Pf*FKBP35 levels are lethal to *P. falciparum* and result in a delayed death-like phenotype that is characterized by perturbed ribosome homeostasis and defective protein synthesis, which is likely linked to the reduced biogenesis of functional ribosomes in the nucleolus. We further found no evidence that FKBP-binding drugs, including FK506, exert their parasiticidal activity in a *Pf*FKBP35-dependent manner, urging strong caution for the future development of FKBP-targeting antimalarials, especially when based on FK506 and structural derivatives thereof. In addition to revealing first insights into the essential function of *Pf*FKBP35 in ribosome homeostasis of *P. falciparum*, we are convinced that the presented data offer valuable information for target-based efforts in malaria drug discovery.

4 Methods

4.1 Parasite culture

P. falciparum culture and synchronization was performed as described (58, 59). Parasites were cultured in AB+ or B+ human red blood cells (Blood Donation Center, Zürich, Switzerland) at a hematocrit of 5% in culture medium containing 10.44 g/L RPMI-1640, 25 mM HEPES, 100 µM hypoxanthine, 24 mM sodium bicarbonate, 0.5% AlbuMAX II (Gibco #11021-037), 0.1 g/L neomycin, and 2 mM choline chloride (Sigma #C7527). To achieve stabilization of DD-tagged proteins in the cell lines NF54/iKD-FKBP35 and NF54/iOE-FKBP35, parasites were cultured in presence of 625 nM Shield-1 (30, 31). To induce the DiCre-mediated recombination of *loxP* sites in NF54/iKO-FKBP35 parasites, cultures were split and treated for 4 h with 100 nM rapamycin or the corresponding volume DMSO, which served as vehicle control, giving rise to FKBP35$^{\mathbf{KO}}$ and FKBP35$^{\mathbf{WT}}$ populations, respectively (32). Cultures were gassed with 3% O_2, 4% CO_2 and 93% N_2 and incubated in an airtight incubation chamber at 37°C.

4.2 Cloning of transfection constructs

CRISPR/Cas9-based gene editing of the NF54 parasites was performed using a two-plasmid approach as previously described (60, 61). This system is based on co-transfection of a plasmid that contains the expression cassettes for the Cas9 enzyme, the single guide RNA (sgRNA) and the blasticidin deaminase (BSD) resistance marker (pBF-gC), and a pD-derived donor plasmid that contains the template for the homology-directed repair of the Cas9-induced DNA double strand break (Fig. S2A) (61).

The plasmids pBF-gC_FKBP-3', pBF-gC_FKBP-5' and pBF-gC_P230p targeting the 3' or 5' end of *fkbp35* (PF3D7_1247400) or the *p230p* (PF3D7_0208900) locus (62), respectively, were generated by ligation of two annealed oligonucleotides (gRNA_top and gRNA_bottom) into the BsaI-digested pBF-gC backbone (61) using T4 DNA ligase (New England Biolabs).

The donor plasmid pD_FKBP35-iKO was generated by assembling six DNA fragments in a Gibson reaction (63) using (i) the plasmid backbone amplified by polymerase chain reaction (PCR) from pUC19 (primers PCRa_F/PCRa_R) (61), (ii/iii) the 5' and 3' homology regions amplified from genomic DNA (primers PCRb_F/PCRb_R and PCRc_F/PCRc_R, respectively), (iv) the *green fluorescent protein* (*gfp*) sequence amplified from pHcamGDV1-GFP-DD (primers PCRd_F/PCRd_R) (61), (v) the HRPII terminator amplified from genomic DNA (primers PCRe_F/PCRe_R), and (vi) the *fkbp35* sequence containing an artificial *loxPint*

(33) amplified from a *P. falciparum* codon-optimized synthetic sequence (primers PCRf_F/PCRf_R) ordered from Genscript.

The donor plasmid pD_FKBP35-iKD was generated by assembling five DNA fragments in a Gibson reaction (63) using (i) the plasmid backbone amplified from pUC19 (primers PCRa_F/PCRa_R) (61), (ii/iii) the 5' and 3' homology regions amplified from genomic DNA (primers PCRg_F/PCRg_R and PCRh_F/PCRh_R, respectively), (iv) the *gfp* sequence amplified from pHcamGDV1-GFP-DD (primers PCRi_F/PCRi_R) (61), and (v) the destabilization domain (*dd*) sequence amplified from pHcamGDV1-GFP-DD (primers PCRj_F/PCRj_R) (61).

The donor plasmid pD_FKBP35-iOE was generated by assembling three DNA fragments in a Gibson reaction (63) using (i) the NheI/PstI-digested plasmid pkiwi003 (64), (ii) the *fkbp35* coding sequence amplified from genomic DNA (primers PCRk_F/PCRk_R), and (iii) the *gfp-dd* sequence amplified from pHcamGDV1-GFP-DD (primers PCRl_F/PCRl_R) (61).

Oligonucleotides are listed in Table S4.

4.3 Transfection and selection of gene-edited parasites

P. falciparum transfection using the CRISPR/Cas9 two-plasmid approach was performed as described previously (61). Briefly, 50 µg of each plasmid (pBF-gC_FKBP-3' and pD_FKBP35-iKO, pBF-gC_FKBP-5' and pD_FKBP35-iKD, pBF-gC_P230p and pD_FKBP35-iOE) were co-transfected into an NF54::DiCre line (65), in which *ap2-g* was tagged with the fluorophore mScarlet as described previously (66). Transgenic parasites were selected with 2.5 µg/mL blasticidin-S-hydrochloride, which was added 24 h after transfection for 10 days. Transgenic populations were usually obtained 2-3 weeks after transfection and correct editing of the modified loci was confirmed by PCR on gDNA (Figs. S1B, S2B and S4B). Primer sequences used for these PCRs are listed in Table S4. Clonal parasite lines were obtained by limiting dilution cloning (67).

4.4 DNA content analysis

NF54/iKO-FKBP35 parasites were fixed in 4% formaldehyde/0.0075% glutaraldehyde for 30 min at room temperature and washed 3 times in PBS and stored at 4°C. Samples were collected

from three independent biological replicates. RNA was digested by incubation with 0.1 mg/mL RNAse A in PBS containing 0.1% Triton-X100 for 15 min at room temperature. Nuclei were stained using 1X SYBR Green 1 DNA stain (Invitrogen S7563) for 20 min and washed three times in PBS. The fixation step quenched the GFP signal detected by the flow cytometer (Fig. S9). SYBR Green intensity was measured using a MACS Quant Analyzer 10 and analyzed using the FlowJo_v10.6.1 software.

4.5 Western blotting

Saponin lysis of 500 µL infected red blood cells at 3-5% parasitaemia was performed by incubation for 10 min on ice in 3 mL ice-cold 0.15% saponin in PBS. The parasite pellets were washed two times in ice-cold PBS and resuspended in Laemmli buffer (62.5 mM Tris base, 2% SDS, 10% glycerol and 5% 2-mercaptoethanol). Proteins were separated on 4-12% Bis-Tris gels (Novex, Qiagen) using MOPS running buffer (Novex, Qiagen). Then proteins were transferred to a nitrocellulose membrane (GE healthcare #106000169), which was blocked with 5% milk powder in PBS/0.1% Tween (PBS-T) for 1 h. The membrane was probed using the primary antibodies mAb mouse α-GFP (1:1’000, Roche Diagnostics #11814460001), mAb mouse α-*Pf*GAPDH (1:20’000) (68), or mAb mouse α-puromycin (1:5’000, Sigma MABE343) diluted in blocking solution. After 2 h incubation, the membrane was washed 5 times in PBS-T before it was incubated with the secondary antibody goat α-mouse IgG (H&L)-HRP (1:10’000, GE healthcare #NXA931). After 1 h incubation, the membrane was washed 5 times and the signal was detected using the chemiluminescent substrate SuperSignal West Pico Plus (Thermo Scientific, REF 34580) and the imaging system Vilber Fusion FX7 Edge 17.10 SN. Nitrocellulose membranes were stripped by incubating for 10 min in a stripping buffer (1 g/L SDS, 15 g/L glycine, 1% Tween-20, pH 2.2) and washed three times in PBS-T before blocking and re-probing.

4.6 Drug dose-response experiments

Dose-response relationships were assessed by exposing synchronous ring stage parasites at 0.5% parasitaemia and 1.25% hematocrit to 12 drug concentrations using a two-step serial dilution in 96-well plates (Corning Incorporated, 96-well cell culture plate, flat bottom, REF 3596) in three independent biological replicates. The plates were gassed and incubated for 48 h at 37 °C. FK506 (MedChemExpress HY-13756), D44 (ChemBridge 7934155 and ChemDiv

7286-2836) and cyclosporin A (Sigma 30024) stocks of 10 mM were prepared in DMSO and working solutions were prepared immediately before the experiment. To measure parasite survival using flow cytometry, cultures were stained in 1X SYBR Green 1 DNA stain (Invitrogen S7563) in a new 96-well plate (Corning Incorporated, 96-well cell culture plate, round bottom, REF 3788) and incubated in the dark for 20 min. The samples were washed once in PBS. Using a MACS Quant Analyzer 10, 50'000 events per condition were measured and analyzed using the FlowJo_v10.6.1 software. Infected RBCs were identified based on SYBR Green 1 DNA stain intensity. The gating strategy is shown in Fig. S9. To quantify parasite survival based on hypoxanthine incorporation into DNA, compounds were dissolved in DMSO (10 mM), diluted in hypoxanthine-free culture medium and titrated in duplicates over a 64-fold range (6 step twofold dilutions) in 96 well plates. 100 µl asexual parasite culture (prepared in hypoxanthine-free medium) were added to each well and mixed with the compound to obtain a final haematocrit of 1.25% and a final parasitemia of 0.3%. After incubation for 48 hrs, 0.25 µCi of [3H]-hypoxanthine was added per well and plates were incubated for an additional 24 hrs. Parasites were then harvested onto glass-fiber filters using a Microbeta FilterMate cell harvester (Perkin Elmer, Waltham, US) and radioactivity was counted using a MicroBeta2 liquid scintillation counter (Perkin Elmer, Waltham, US). The results were recorded and expressed as a percentage of the untreated controls. Curve fitting and IC50 calculations were performed using a non-linear, four-parameter regression model with variable slope (Graph Pad Prism, version 8.2.1).

4.7 Fluorescence microscopy

To localize *Pf*FKBP35, NF54/iKD-FKBP35 parasites were fixed in 4% formaldehyde/0.0075% glutaraldehyde for 30 min at room temperature and washed three times in PBS. The fixed cells were permeabilized by incubation with 0.1% Triton-X100-containing PBS for 15 min. After two washing steps in PBS, the cells were incubated in a blocking/aldehyde quenching solution (3% BSA in PBS complemented with 50 mM ammonium chloride). The samples were incubated with the primary antibodies rabbit α-GFP (1:400, Abcam ab6556) and mAb mouse α-fibrillarin (1:100, Santa Cruz Biotechnology sc-166021) for 1 h in 3% BSA in PBS and washed 3 times in PBS. Subsequently, the samples were incubated with the secondary antibodies goat α-rabbit IgG (H&L) Alexa Fluor 488 (1:250, Invitrogen A11008) and goat α-mouse IgG (H&L) Alexa Fluor 594 (1:250, Invitrogen A11032), for 1 h and washed 3 times, before they were mixed with Vectashield containing DAPI (Vector laboratories, H-1200), and

mounted on a microscopy slide. Slides were imaged using a Leica THUNDER 3D Assay imaging system.

4.8 Proteomics

Parasite cultures were split at 0-6 hpi in G1 and treated for 4 h with 100 nM rapamycin. Saponin lysis of paired FKBP35^{WT} and FKBP35^{KO} populations at 36-42 hpi in G1 and 24-30 hpi in G2 was performed as described above. Samples were collected in three independent biological replicates. The washed parasite pellet was snap frozen in liquid nitrogen. After thawing, parasites were resuspended in 25 µL of lysis buffer (5% SDS, 100 mM tetraethylammonium bromide (TEAB), 10 mM tris(2-carboxyethyl)phosphin (TCEP), pH 8.5) and sonicated (10 cycles, 30 sec on/off at 4 °C, Bioruptor, Diagnode). Lysates were subsequently reduced for 10 minutes at 95 °C. Samples were then cooled down to RT and 0.5 µL of 1M iodoacetamide was added to the samples. Cysteine residues were alkylated for 30 min at 25 °C in the dark. Digestion and peptide purification was performed using S-trap technology (Protifi) according to the manufacturer's instructions. In brief, samples were acidified by addition of 2.5 µL of 12% phosphoric acid (1:10) and then 165 µL of S-trap buffer (90% methanol, 100 mM TEAB pH 7.1) was added to the samples (6:1). Samples were briefly vortexed and loaded onto S-trap micro spin-columns (Protifi) and centrifuged for 1 min at 4000 g. Flow-through was discarded and spin-columns were then washed 3 times with 150 µL of S-trap buffer (each time samples were centrifuged for 1 min at 4000 g and flow-through was removed). S-trap columns were then moved to the clean tubes and 20 µL of digestion buffer (50 mM TEAB pH 8.0) and trypsin (at 1:25 enzyme to protein ratio) were added to the samples. Digestion was allowed to proceed for 1h at 47 °C. Then, 40 µL of digestion buffer were added to the samples and the peptides were collected by centrifugation at 4000 g for 1 minute. To increase the recovery, S-trap columns were washed with 40 µL of 0.2% formic acid in water (400g, 1 min) and 35 µL of 0.2% formic acid in 50% acetonitrile. Eluted peptides were dried under vacuum and stored at -20 °C until further analysis.

Peptides were resuspended in 0.1% aqueous formic acid and peptide concentration was adjusted to 0.25 µg/µL. 1 µL of each sample was subjected to LC-MS/MS analysis using an Orbitrap Elicpse Tribrid Mass Spectrometer fitted with an Ultimate 3000 nano system (both from Thermo Fisher Scientific) and a custom-made column heater set to 60 °C. Peptides were resolved using a RP-HPLC column (75 µm × 30 cm) packed in-house with C18 resin (ReproSil-

Pur C18–AQ, 1.9 µm resin; Dr. Maisch GmbH) at a flow rate of 0.3 µL/min. The following gradient was used for peptide separation: from 2% buffer B to 12% B over 5 min, to 30% B over 40 min, to 50% B over 15 min, to 95% B over 2 min followed by 11 min at 95% B then back to 2% B. Buffer A was 0.1% formic acid in water and buffer B was 80% acetonitrile, 0.1% formic acid in water.

The mass spectrometer was operated in DDA mode with a cycle time of 3 seconds between master scans. Each master scan was acquired in the Orbitrap at a resolution of 240,000 FWHM (at 200 m/z) and a scan range from 375 to 1600 m/z followed by MS2 scans of the most intense precursors in the linear ion trap at "Rapid" scan rate with isolation width of the quadrupole set to 1.4 m/z. Maximum ion injection time was set to 50 ms (MS1) and 35 ms (MS2) with an AGC target set to 1e6 and 1e4, respectively. Only peptides with charge state 2-5 were included in the analysis. Monoisotopic precursor selection (MIPS) was set to Peptide, and the Intensity Threshold was set to 5e3. Peptides were fragmented by HCD (Higher-energy collisional dissociation) with collision energy set to 35%, and one microscan was acquired for each spectrum. The dynamic exclusion duration was set to 30 seconds.

The acquired raw-files were imported into the Progenesis QI software (v2.0, Nonlinear Dynamics Limited), which was used to extract peptide precursor ion intensities across all samples applying the default parameters. The generated mgf-file was searched using MASCOT against a *Plasmodium falciparum* (isolate 3D7) database (Uniprot, 11.2019) and 392 commonly observed contaminants using the following search criteria: full tryptic specificity was required (cleavage after lysine or arginine residues, unless followed by proline); 3 missed cleavages were allowed; carbamidomethylation (C) was set as fixed modification; oxidation (M) and acetyl (Protein N-term) were applied as variable modifications; mass tolerance of 10 ppm (precursor) and 0.6 Da (fragments). The database search results were filtered using the ion score to set the false discovery rate (FDR) to 1% on the peptide and protein level, respectively, based on the number of reverse protein sequence hits in the dataset. Quantitative analysis results from label-free quantification were processed using the SafeQuant R package v.2.3.2 (69) to obtain peptide relative abundances. This analysis included global data normalization by equalizing the total peak/reporter areas across all LC-MS runs, data imputation using the knn algorithm, summation of peak areas per protein and LC-MS/MS run, followed by calculation of peptide abundance ratios. Only isoform specific peptide ion signals were considered for quantification. To meet additional assumptions (normality and homoscedasticity) underlying the use of linear regression models and t-Tests, MS-intensity signals were transformed from the linear to the

log-scale. The summarized peptide expression values were used for statistical testing of between condition differentially abundant peptides. Here, empirical Bayes moderated t-Tests were applied, as implemented in the R/Bioconductor limma package (70). The resulting per protein and condition comparison *p*-values were adjusted for multiple testing using the Benjamini-Hochberg method.

Gene ontology enrichment analysis was performed using the PANTHER Overrepresentation Test with the correction method “False Discovery Rate”, the test type “Fisher's Exact”, and the annotation data set “PANTHER GO-Slim” (37).

4.9 IPP complementation

Parasite cultures were split at 0-6 hpi in G1 and treated for 4 h with 100 nM rapamycin. FKBP35$^{\mathbf{KO}}$ and FKBP35$^{\mathbf{WT}}$ populations were split again and supplemented either with 200 µM isopentenyl pyrophosphate (IPP) (Sigma I0503) or the corresponding volume H_2O. The respective culture medium was replaced daily. Parasites treated with 156 ng/mL doxycycline (Sigma D9891) were used to confirm that IPP complementation is able to rescue apicoplast-deficient parasites. DNA content analysis was performed as described above.

4.10 Heat shock susceptibility testing

Parasites cultures were split at 0-6 hpi in G1 and treated for 4 h with 100 nM rapamycin. While control populations were always incubated at 37 °C, test populations were incubated at 40 °C for 6 h starting at 24-30 hpi. Parasitaemia was measured in G2 using flow cytometry as described above.

4.11 Surface sensing of translation (SUnSET)

Parasite cultures were split at 0-6 hpi in G1 and treated for 4 h with 100 nM rapamycin. At 24-30 hpi in G2, the cultures were incubated with 1 µg/mL puromycin (Sigma P8833) for 1 h at 37 °C (41, 71). Saponin lysis and Western blotting were performed as described above.

4.12 Cellular thermal shift assay (CETSA)

The mass spectrometry-based isothermal dose-response cellular thermal shift assay (ITDR-MS-CETSA) was performed according to the protocol developed by Dziekan and colleagues (47). Briefly, live parasites (10^7 MACS-purified trophozoites per condition) were exposed to a FK506 (MedChemExpress HY-13756) concentration gradient (100 µM to 1.5 nM) and a DMSO control for 1 h. Subsequently, the parasites were washed in PBS and exposed to the denaturing temperatures 50 °C, 55 °C and 60 °C as well as to a non-denaturing temperature 37 °C for 3 min, before they were cooled down to 4 °C for 3 min. Afterwards, the cells were lysed by resuspending in a lysis buffer (50 mM HEPES pH 7.5, 5 mM β-glycerophosphate, 0.1 mM Na_3VO_4, 10 mM $MgCl_2$, 2 mM TCEP, and EDTA-free protease inhibitor cocktail (Sigma)), three freeze/thaw cycles, and mechanical shearing using a syringe with a 31-gauge needle. Subsequently, insoluble proteins were pelleted by centrifugation (20 min at 4 °C and 20’000 g) and the soluble fraction was collected and subjected to protein digestion, reduction, alkylation, and TMT10 labelling followed by LC/MS analysis as described (47).

To prepare the protein lysate, saponin-lysed parasites were lysed in the afore-mentioned buffer by three freeze/thaw cycles and mechanical shearing. After centrifugation, soluble proteins were exposed to a FK506 concentration gradient (200 µM to 3 nM) and a DMSO control for 1 min before the thermal challenge was performed as described above. Afterwards, the soluble protein fraction was isolated and prepared for by LC/MS analysis as described (47).

Data analysis was performed using the Proteome Discoverer 2.1 software (Thermo Fisher Scientific) and the R package “mineCETSA” (v 1.1.1). Only proteins identified by at least three peptide spectrum matches (PSMs) were included in the analysis (47).

4.13 Transcriptomics

4.13.1 Sample preparation

The RNA of 500 µL iRBCs at 3-5% parasitaemia was isolated using 3 mL TRIzol reagent (Invitrogen) followed by phenol-chloroform phase separation. The aqueous phase was purified using the Direct-zol RNA MicroPrep kit (Zymo). Samples were collected from three biological replicates. Stranded RNA sequencing libraries were prepared using the Illumina TruSeq stranded mRNA library preparation kit (REF 20020594) according to the manufacturer’s protocol. The library was sequenced in 100 bp paired-end reads on an Illumina NextSeq 2000

sequencer using the Illumina NextSeq 2000 P3 reagents (REF 20040560), resulting in 5 million reads on average per sample.

4.13.2 RNA-Seq data analysis

Fastqc was run on all raw fastq files. Then, each file was aligned with hisat2 (version 2.0.5) (72) against the 3D7 reference genome (PlasmoDB v58) (73) in which the GFP and the recoded FBPK35 sequences were added at the end of chromosome 12. Read counts for each gene and for each sample were then counted using featureCount (gff file from PlasmoDB v58 modified to include the added GFP and FBPK35). TPM (Transcripts Per Kilobase Million) were then calculated from the raw count matrix.

Principal component analysis (PCA) was performed using the R (version 4.2.1) function prcomp using log transformed TPMs. PCA revealed that the rapamycin-treated replicate B of TP 3 ("3B.R") was a clear outlier and is different from any other replicate at any time point (Fig. S3D). For this reason, it was excluded from further analysis. The PCA was done again without it and the other samples show the same pattern as the initial PCA (Fig. S3E).

DESeq2 (version 1.36) (74) was used for normalization and differential expression analysis. Paired differential expression tests where done for each time point using DESeq2 LRT (likelihood ratio test) using the full model ~ Treatment + Replicate (Treatment is DMSO or Rapamycin and Replicate is the clone, added as the data is paired) and the reduced model ~ Replicate. From this paired test and the average log fold-change calculated from the TPMs, normalized volcano plots were made using the R package EnhancedVolcano (version 1.14) (75).

4.13.3 Cell cycle analysis

Spearman correlation between normalized scaled read counts for each sample for all genes (as one vector) and each time point of the reference microarray time course published by Bozdech *et al.* (42) (3D7 smoothed, retrieved from PlasmoDB) were tested. Spearman's coefficients rho for each time point of this RNA-Seq time course and each time point of the reference data set where plotted using ggcorrplot (version 0.1.3) (76). For each time point of this RNA-Seq dataset, the rho coefficients where then plotted against the time points of the reference data set and the FKBP35^{WT} and FKBP35^{KO} data were fitted separately to the linearized sinusoidal $A * sin\left(\frac{2\pi}{53} time\right) + B * cos\left(\frac{2\pi}{53} time\right) + C$ using R lm function. The time point matching best to the FKBP35$^{\mathbf{WT}}$ and FKBP35$^{\mathbf{KO}}$ samples for each time point of the RNA-Seq time course was

taken as the maximum of this fitted function. Both fitted functions were F-tested (using R function var.test using both fitted model as applied to the FKBP35$^{\mathbf{KO}}$ data) to test whether the FKBP35$^{\mathbf{WT}}$ and FKBP35$^{\mathbf{KO}}$ data correlated with the reference data set (42) in a significantly different way, which would indicate a cell cycle shift if statistically significant. Only the last time point showed such a significant difference.

Data availability

The mass spectrometry proteomics data have been deposited to the ProteomeXchange Consortium repository with the dataset identifier PXD039018. The sequencing data are available in the Sequence Read Archive (SRA) via the accession number PRJNA914079.

Acknowledgements

We thank Vera Mitesser and Ron Dzikowski for guidance on the SUnSET experiments and David Fidock for providing the parasite line Dd2-B2 used for the attempted resistance selection. We are grateful to the Polyomics facility at the University of Glasgow for processing the samples for RNA-Seq. This work was supported by the Swiss National Foundation (grant number 310030_200683), the Wolfson Merit Royal Society Award, the Wellcome Trust Investigator Award 110166 and Wellcome Trust Center Award 104111, and by the Singapore Ministry of Education (grant number MOE-T2EP30120-0015).

Author contributions

B.T.T. designed and performed experiments, analyzed and interpreted the data, and wrote the original draft of the manuscript. J.M.D. and S.T. performed and interpreted CETSA experiments. Z.B. supervised these experiments and provided resources. F.A. analyzed RNA-Seq data. M.M. supervised these experiments and provided resources for RNA-Seq data generation. A.P. performed immunofluorescence assays. K.B. performed and analyzed proteomics experiments supervised by A.S. C.Gu. and M.R. performed and interpreted hypoxanthine incorporation assays. C.Gr. edited the manuscript. N.M.B.B. conceived the study, designed and supervised experiments, provided resources, and wrote the manuscript. All authors contributed to the final editing of the manuscript.

Declaration of interests

The authors declare that they have no conflict of interest.

Figures

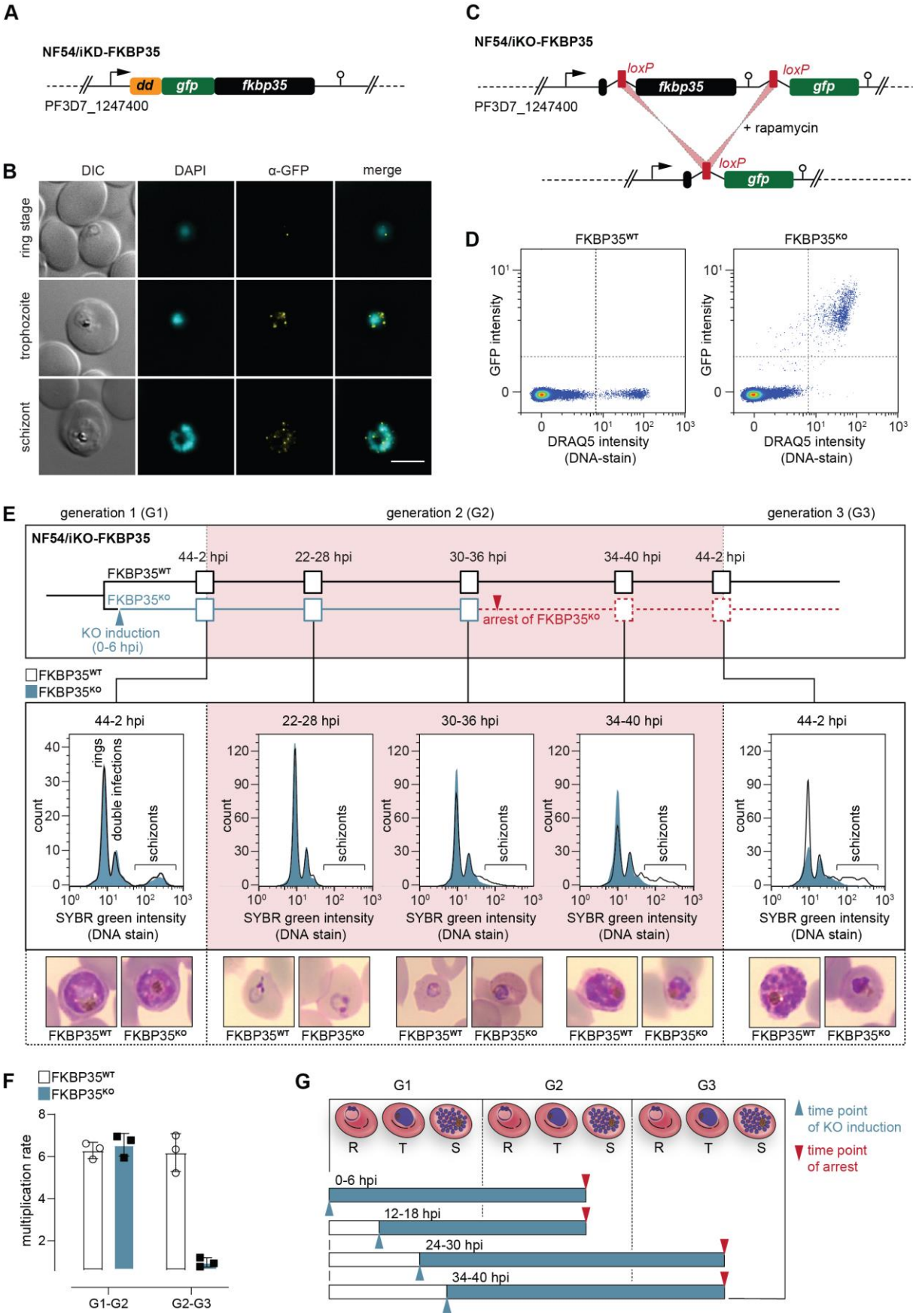
A
NF54/iKD-FKBP35
dd
gfp
fkbp35
PF3D7_1247400
B
DIC
DAPI
α-GFP
merge
ring stage
trophozoite
schizont
C
NF54/iKO-FKBP35
loxP
fkbp35
gfp
PF3D7_1247400
+ rapamycin
D
FKBP35WT
FKBP35KO
GFP intensity
DRAQ5 intensity
(DNA-stain)
E
generation 1 (G1)
generation 2 (G2)
generation 3 (G3)
NF54/iKO-FKBP35
44-2 hpi
22-28 hpi
30-36 hpi
34-40 hpi
44-2 hpi
FKBP35WT
FKBP35KO
KO induction
(0-6 hpi)
arrest of FKBP35KO
rings
double infections
schizonts
count
SYBR green intensity
(DNA stain)
F
multiplication rate
G1-G2
G2-G3
G
G1
G2
G3
R
T
S
time point
of KO induction
time point
of arrest
0-6 hpi
12-18 hpi
24-30 hpi
34-40 hpi

Figure 1. *Pf*FKBP35 depletion causes delayed parasite death.

(A) Schematic of the N-terminally modified *fkbp35* locus in NF54/iKD-FKBP35 parasites. *dd*, destabilization domain. *gfp, green fluorescent protein*. **(B)** Localization of *Pf*FKBP35 in NF54/iKD-FKBP35 parasites at the ring, trophozoite and schizont stage assessed by immunofluorescence. DNA was stained with DAPI. Representative images are shown. Scale bar: 5 µm. DIC, differential interference contrast.**(C)** Schematic of the modified *fkbp35* locus in NF54/iKO-FKBP35 parasites before and after *loxP* recombination. *gfp, green fluorescent protein*. **(D)** Flow cytometry plot showing GFP expression in G1 schizonts of FKBP35$^{\mathbf{KO}}$ and FKBP35$^{\mathbf{WT}}$. DNA was stained with DRAQ5. **(E)** Time course showing the development of NF54/iKO-FKBP35 parasites. Upper panel: Schematic of the experimental setup. Middle panel: DNA content of the populations assessed by flow cytometry based on the SYBR Green intensity. Lower panel: Giemsa-stained blood smears. The knockout was induced at 0-6 hpi. Representative data of three biological replicates are shown. **(F)** Multiplication rates of FKBP35$^{\mathbf{KO}}$ and FKBP35$^{\mathbf{WT}}$ parasites from generation 1 to generation 2 (G1-G2) and G2-G3. The knockout was induced at 0-6 hpi. Multiplication rates were determined using flow cytometry. Data points represent the multiplication rates from G1-G2 and G2-G3. n=3, error bars represent the standard error of the mean. **(G)** Schematic showing time point of growth arrest (red arrow) following *Pf*FKBP35 knock-out at different hpi (blue arrow). R, ring stage; T, trophozoite stage; S, schizont stage.

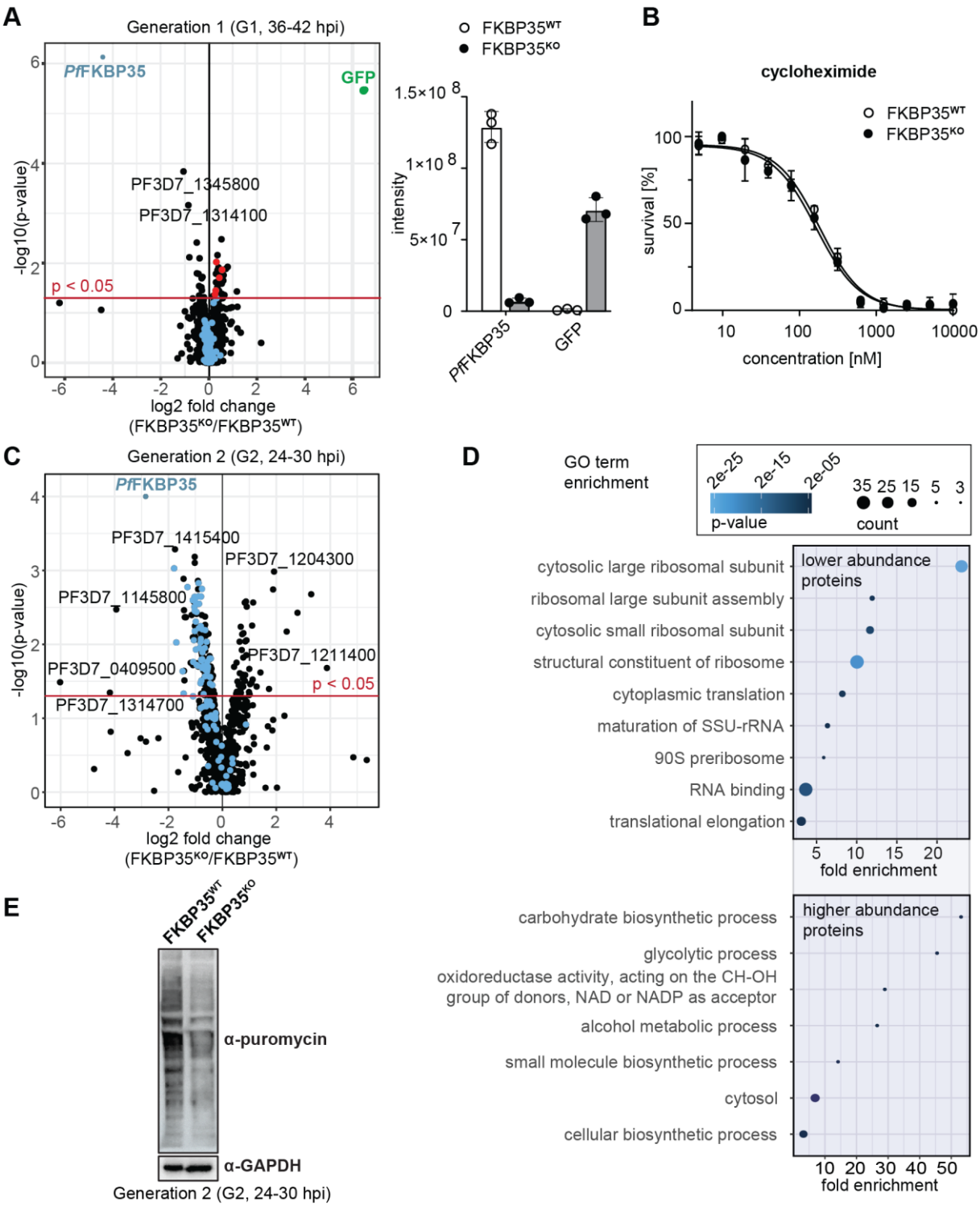

Figure 2. *Pf*FKBP35 is crucial for ribosome homeostasis and protein synthesis.

(A) Left panel: Proteome analysis of schizonts (36-42 hpi) in G1. The volcano plot shows change in protein abundance in FKBP35^{KO} compared to FKBP35^{WT}. Ribosomal proteins are highlighted in blue, proteins associated with the GO terms "pre-ribosome" or "nucleolus" in red. n=3. Right panel: Relative difference in *Pf*FKBP35 and GFP abundance expressed as signal intensity measured by mass spectrometry. n=3, error bars represent the standard error of the

mean. **(B)** Dose-response effect of the translation inhibitor cycloheximide on FKBP35$^{\mathbf{KO}}$ and FKBP35$^{\mathbf{WT}}$ parasites. The knockout was induced at 0-6 hpi and parasites were subsequently exposed to cycloheximide for 48 h. Parasite survival was quantified by flow cytometry. n=3, error bars represent the standard error of the mean. **(C)** Proteome analysis of trophozoites (24-30 hpi) in G2. The volcano plot shows change in protein abundance in FKBP35$^{\mathbf{KO}}$ compared to FKBP35$^{\mathbf{WT}}$. Ribosomal proteins are highlighted in blue. n=3. **(D)** GO enrichment analysis of significantly deregulated proteins in FKBP35$^{\mathbf{KO}}$ trophozoites in G2. GO enrichment analysis was performed using the PANTHER "Overrepresentation Test" with the test type "Fisher's Exact" and the correction method "False Discovery Rate". **(E)** Assessment of translation activity using SUnSET. FKBP35$^{\mathbf{KO}}$ and FKBP35$^{\mathbf{WT}}$ trophozoites of G2 were incubated with puromycin for 1 hour. Incorporated puromycin was detected using an α-puromycin antibody. α-GAPDH served as loading control. n=3, a representative Western blot is shown.

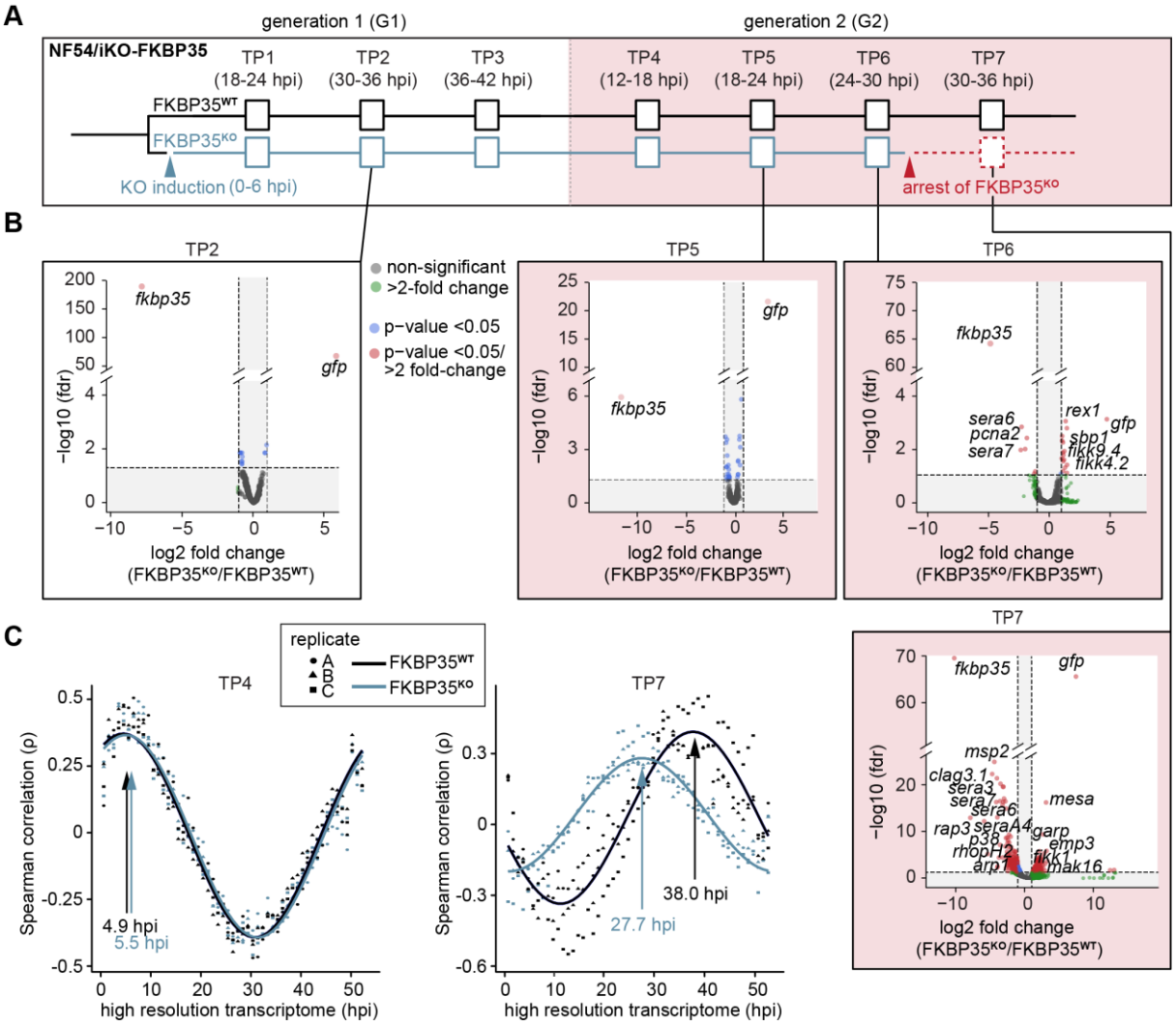

Figure 3. The knockout of *Pf*FKBP35 remains silent at the transcriptomic level.

(A) Setup of the RNA-Seq experiment. RNA was collected at seven indicated time points (TP). **(B)** Volcano plots show differential gene expression between FKBP35^{KO} and FKBP35^{WT} parasites. Genes are color-coded according to the fold change and fdr (false discovery rate), n=3. **(C)** Mapping of FKBP35^{KO} and FKBP35^{WT} transcriptomes to a high-resolution reference (42). Spearman rank coefficients (ρ) show correlation between the sampled transcriptomes and the reference data set (42). The time points with the highest correlation coefficient are indicated.

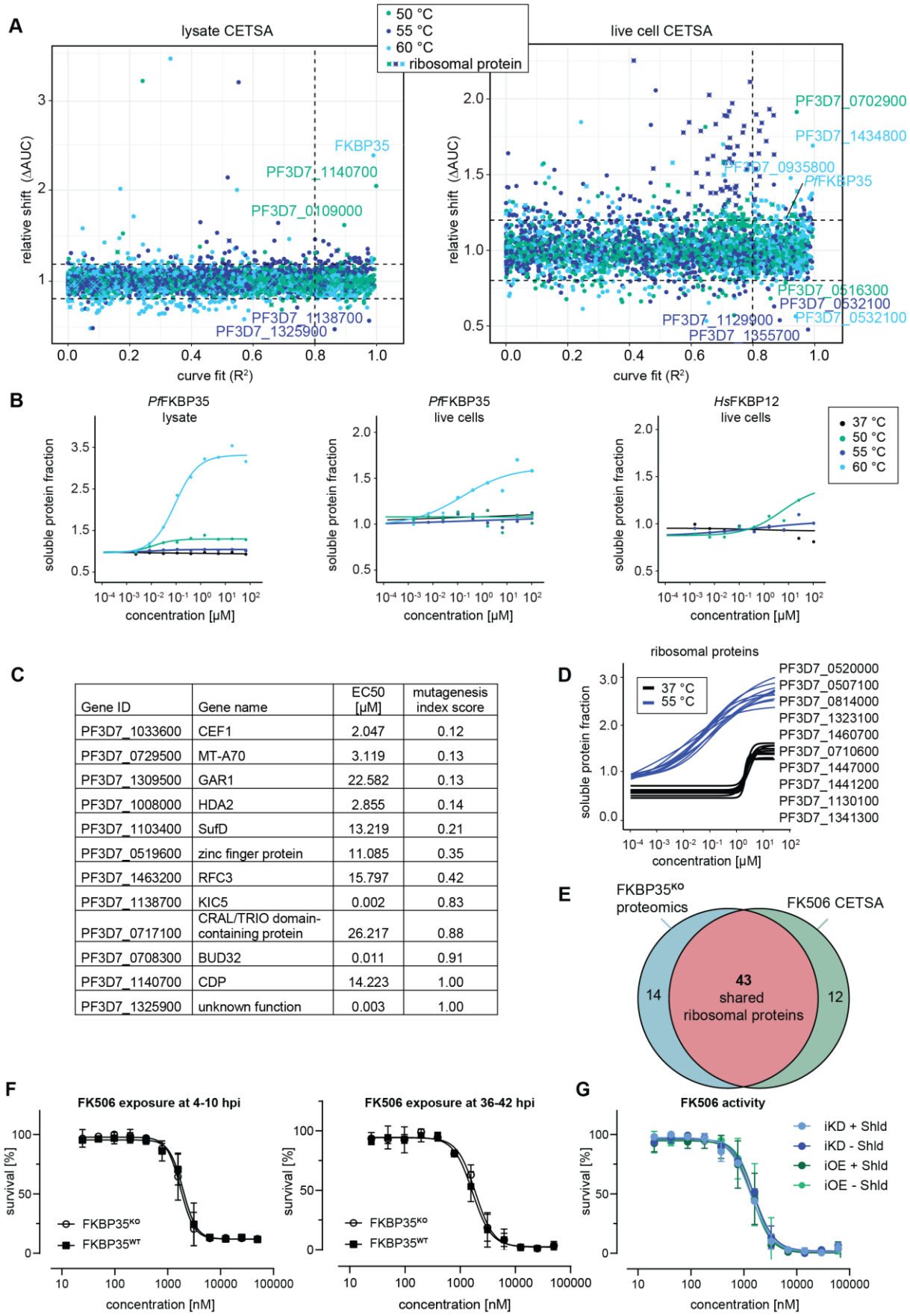

Gene ID	Gene name	EC50 [µM]	mutagenesis index score
PF3D7_1033600	CEF1	2.047	0.12
PF3D7_0729500	MT-A70	3.119	0.13
PF3D7_1309500	GAR1	22.582	0.13
PF3D7_1008000	HDA2	2.855	0.14
PF3D7_1103400	SufD	13.219	0.21
PF3D7_0519600	zinc finger protein	11.085	0.35
PF3D7_1463200	RFC3	15.797	0.42
PF3D7_1138700	KIC5	0.002	0.83
PF3D7_0717100	CRAL/TRIO domain-containing protein	26.217	0.88
PF3D7_0708300	BUD32	0.011	0.91
PF3D7_1140700	CDP	14.223	1.00
PF3D7_1325900	unknown function	0.003	1.00

Figure 4. CETSA identifies FK506 interaction partners.

(A) CETSA results. The relative shift in protein abundance (area under the curve of heat-challenged samples normalized against the non-denaturing control, ΔAUC) as a function of R^2 (goodness of fit as a measure for the dose-response effect). The dashed lines indicate an arbitrary cutoff of 3 times the median absolute deviation (MAD) of each dataset and R^2=0.8. Three different temperatures were used for protein denaturation (indicated by colors). **(B)** Dose-dependent stabilization of *P. falciparum* and human FKBPs detected using lysate and live cell CETSA. Bullets represent the abundance of non-denatured proteins in response to increasing FK506 concentrations under thermal challenge relative to the DMSO control. Colors indicate the temperatures used for heat challenge; the black curve represents the non-denaturing (37°C) control. **(C)** Proteins with the most pronounced stability shift under thermal challenge in the lysate CETSA experiment are listed. The EC50 is the concentration at which the half-maximal effect of the FK506-induced thermal stabilization is reached. The mutagenesis index score determined by Zhang *et al*. (18) is a measure to predict if a protein is essential for asexual growth: 0=essential, 1=non-essential. **(D)** Fitted live cell CETSA curves of 10 representative ribosomal proteins at 37°C and 55°C. Ribosomal proteins show a FK506 dose-dependent increase in soluble protein fraction. **(E)** Venn diagram showing the overlap between ribosomal proteins deregulated in the *Pf*FKBP35 knock-out cell line (less abundant in G2 FKBP$^{\mathbf{KO}}$ trophozoites determined by proteomics) and the ribosomal proteins stabilized by FK506 in live cell CETSA. The number of factors identified in either or both assays is indicated. **(F)** Dose-response effect of FK506 on FKBP35$^{\mathbf{KO}}$ and FKBP35$^{\mathbf{WT}}$ parasites. The knockout was induced at 0-6 hpi and parasites were exposed to FK506 at 4-10 hpi and 36-42 hpi for 48h. n=3, error bars represent the standard error of the mean. **(G)** Dose-response effect of FK506 on NF54/iKD-FKBP35 and NF54/iOE-FKBP35 parasites in presence and absence of Shield-1 (Shld). Parasites were split at 0-6 hpi and subsequently treated with Shld or the vehicle control EtOH. Data points represent the mean of three and two independent biological replicates for the NF54/iOE-FKBP35 and NF54/iKD-FKBP35 cell line, respectively. Error bars represent the standard error of the mean.

Supplemental figures

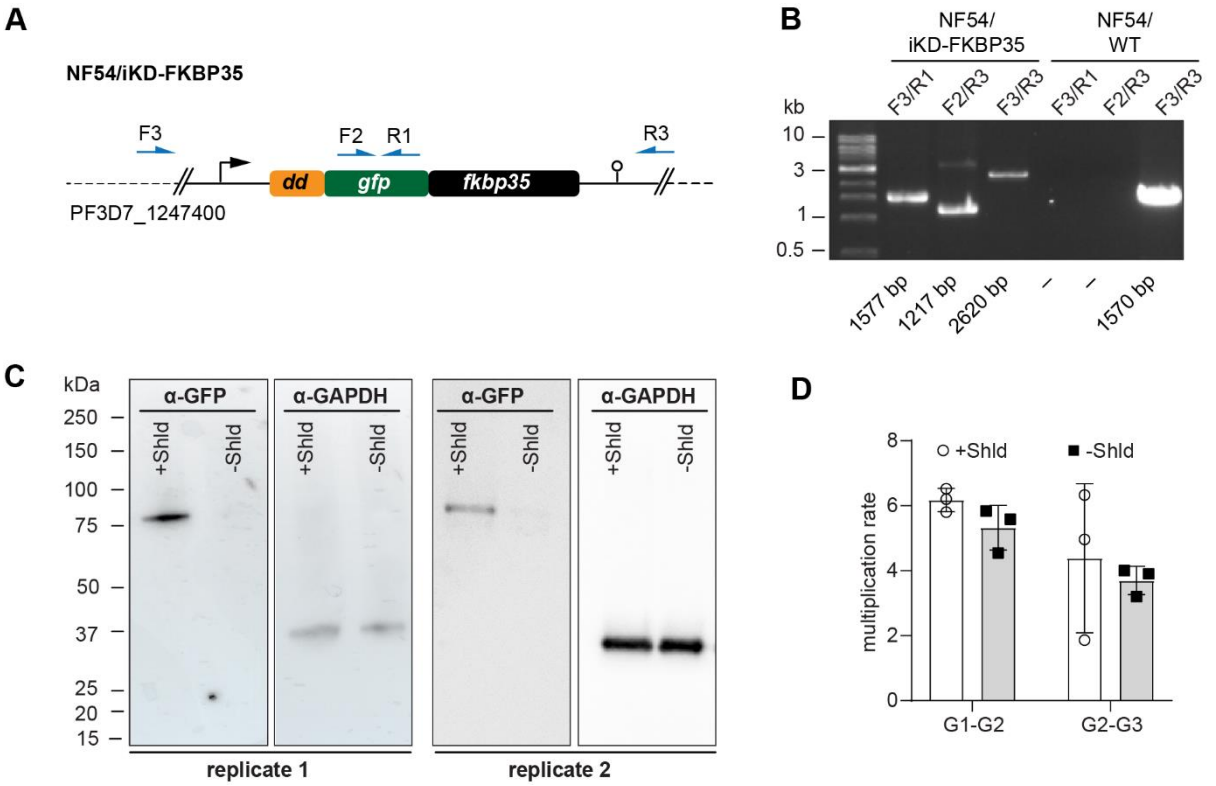

Figure S1. Characterization of NF54/iKD-FKBP35 parasites.

(A) Schematic of the modified *fkbp35* locus (PF3D7_1247400) in NF54/iKD-FKBP35 parasites. The 5'-end of *fkbp35* was tagged with the sequences of a destabilization domain (*dd*) and a green fluorescent protein (*gfp*). The DD tag allows regulating protein levels post-translationally using the stabilizing compound Shield-1 (Shld) (30, 31). Names and binding sites of the primers used for diagnostic PCRs are indicated. **(B)** Diagnostic PCRs performed on gDNA of NF54/FKBP35 iKD parasites to confirm correct editing of the locus. PCRs performed on NF54/WT gDNA served as control. Numbers at the bottom indicate expected fragement sizes. **(C)** Expression levels of the DD-GFP-FKBP35 fusion protein were assessed by Western blot. Parasite cultures were split at 0-6 hpi and treated with Shld or the vehicle control EtOH. Protein lysates were collected 40 hours later. α-GAPDH served as loading control. The expected size of the DD-GFP-FKBP35 fusion protein is 74.2 kDa. **(D)** Multiplication rates of NF54/iKD-FKBP35 parasites from generation 1 to generation 2 (G1-G2) and G2-G3. Parasites were split at 0-6 hpi and treated with Shld or the vehicle control EtOH. Multiplication rates were determined using flow cytometry. Data points represent the multiplication rates from G1-G2 and G2-G3, respectively. n=3; error bars represent the standard error of the mean.

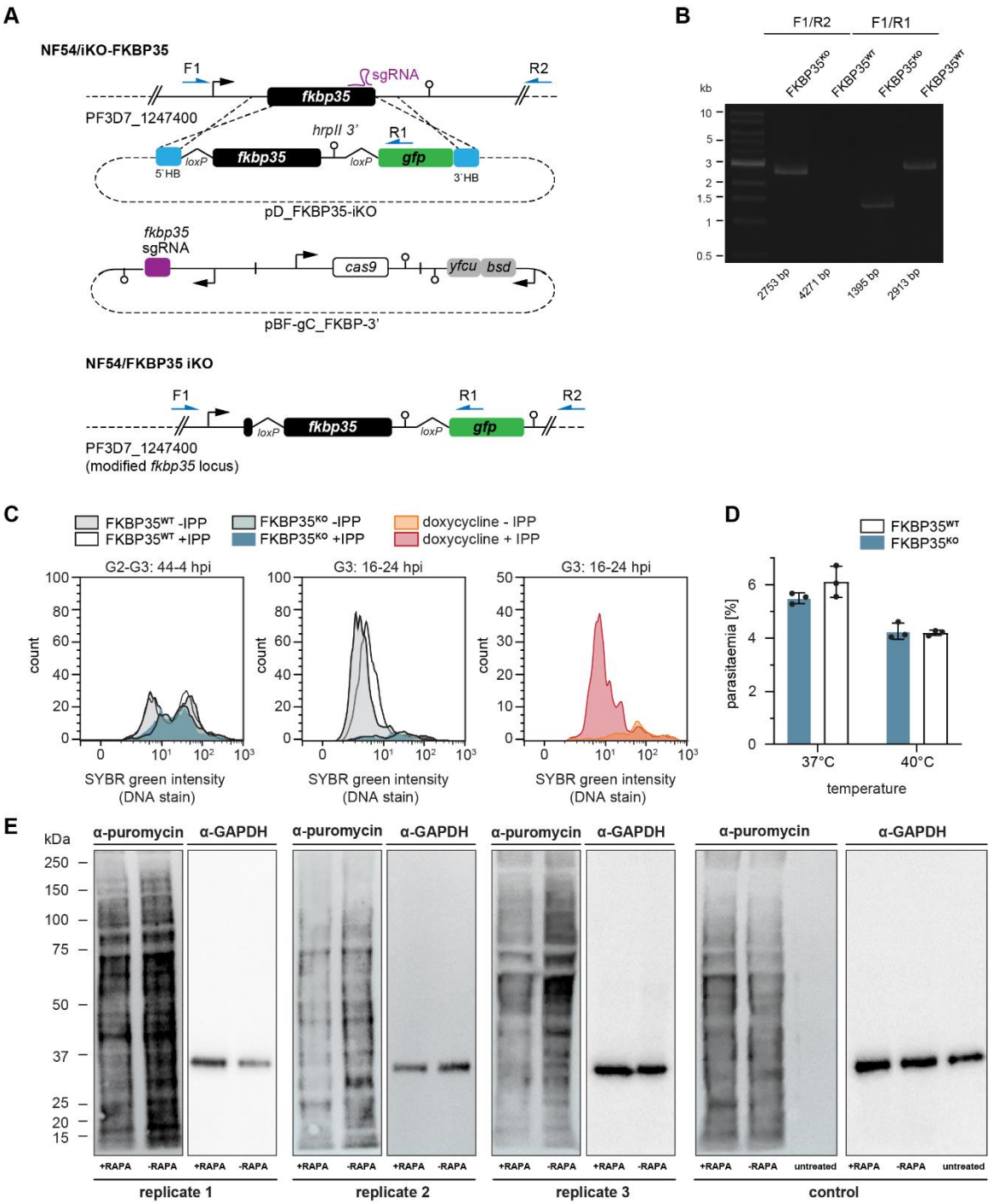

Figure S2. CRISPR/Cas9-based generation of transgenic parasite lines.

(A) Schematic of the wild type *fkbp35* locus (PF3D7_1247400) and the two plasmids used for CRISPR/Cas9 gene editing (pD_FKBP35-iKO and pBF-gC_FKBP-3') to generate the modified *fkbp35* locus of NF54/iKO-FKBP35 parasites. The modification consists of an intron containing a *loxP* site that was introduced after the first 38 bp of the coding sequence and an *hrpII* terminator inserted after the stop codon followed by another *loxP* site and a *gfp* sequence. The sequence flanked by the *loxP* sites was recodonized to prevent homologous recombination during gene editing. Names and binding sites of the primers used for diagnostic PCRs are

indicated. **(B)** Diagnostic PCRs on gDNA of NF54/iKO-FKBP35 parasites confirm correct locus editing and rapamycin-induced *loxP* recombination. Numbers at the bottom indicate the expected band sizes. **(C)** DNA content analysis of FKBP35$^{\mathbf{KO}}$ and FKBP35$^{\mathbf{WT}}$ parasites in presence or absence of isopentenyl pyrophosphate (IPP)-supplementation. Disruption of isoprenoid precursor biosynthesis in the apicoplast – the only essential function of this organelle – is a known cause for delayed death in *P. falciparum* (35, 36). Inhibition of isoprenoid synthesis by doxycycline can thus be restored by supplementing the parasite culture medium with the isoprenoid precursor IPP (77). However, IPP supplementation did not alter the fate of FKBP35$^{\mathbf{KO}}$ cells, demonstrating that their death in G2 is independent of apicoplast-dependent processes as shown by DNA content analysis. Doxycycline-treated wild-type parasites rescued by IPP-supplementation served as positive control**.** The knockout was induced at 0-6 hpi. Representative data of three biological replicates are shown. **(D)** Parasite survival after exposure to 40 °C for 6 h. Given the reported interactions of *Pf*FKBP35 with heat shock protein 70 (HSP70) and HSP90 (14, 16), we tested the parasite`s response to heat stress. *Pf*HSP70 is required to ensure parasite survival under heat shock conditions by stabilizing the digestive vacuole membrane trough binding to phosphatidylinositol 3-phosphate (78). Despite this association, we did not detect altered heat-susceptibility between FKBP35$^{\mathbf{KO}}$ and FKBP35$^{\mathbf{WT}}$ cells. The knockout was induced at 0-6 hpi. n=3, error bars represent the standard error of the mean**. (E)** Assessment of translation rates using SUnSET. FKBP35^{KO} and FKBP35^{WT} trophozoites of G1 were incubated with puromycin for 1 hour. Incorporated puromycin was detected using an α-puromycin antibody; α-GAPDH served as loading control. Replicate 3 is also shown in main figure 3 (mirrored). The control was performed using an NF54/DiCre parasite line. Untreated control parasites were cultured in absence of puromycin, confirming the specificity of the α-puromycin antibody.

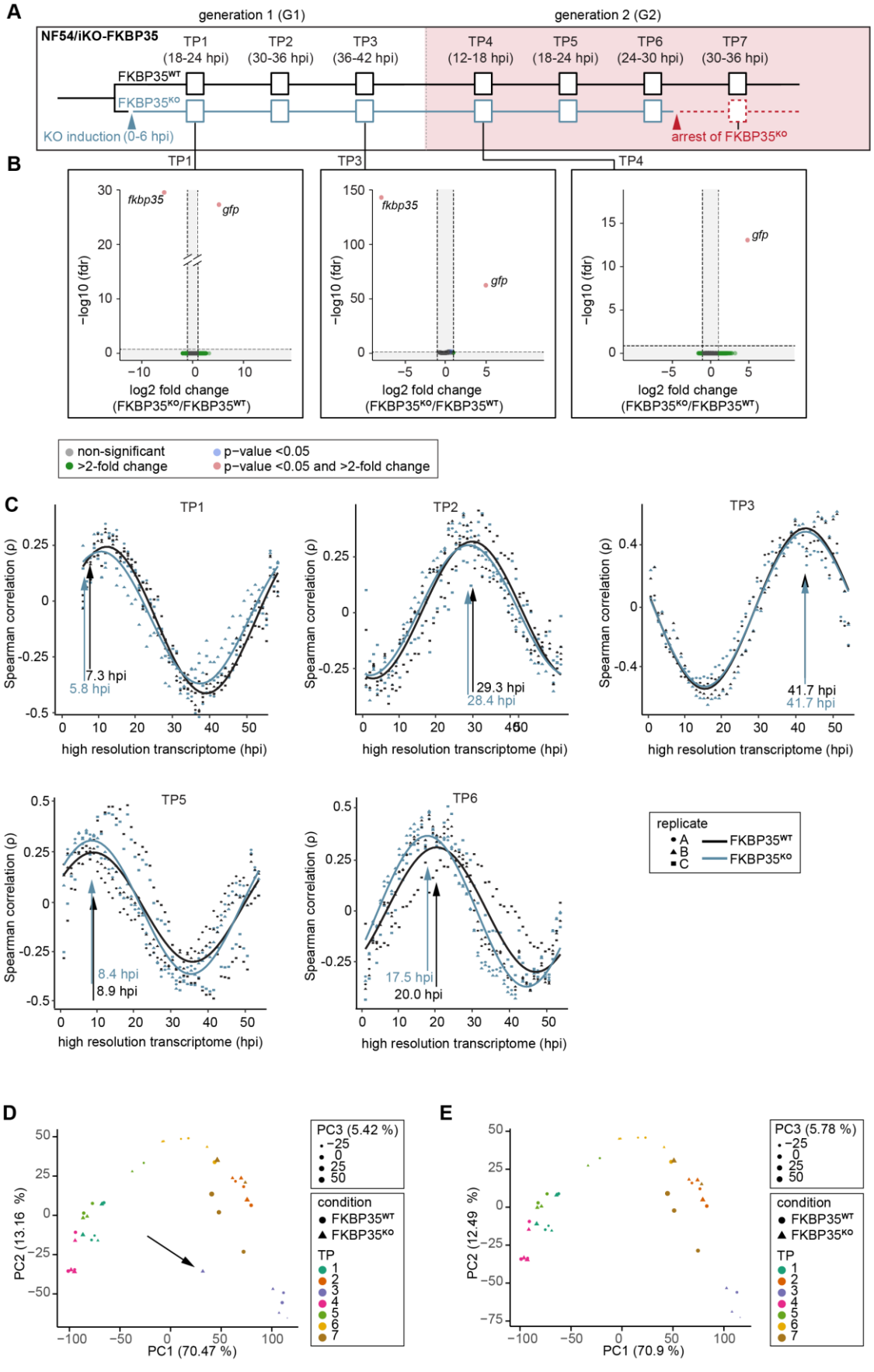

Figure S3. Transcriptomics reveals a cell cycle arrest of FKBP35^{KO} parasites.

(A) Schematic of the experimental setup. The knockout was induced at 0-6 hpi. RNA was collected at indicated time points (TPs). **(B)** Volcano plots show differential gene expression between FKBP35^{KO} and FKBP35^{WT} parasites. Genes are color-coded according to the fold change and fdr (false discovery rate), n=3. **(C)** Mapping of FKBP35$^{\mathbf{KO}}$ and FKBP35$^{\mathbf{WT}}$ transcriptomes to a high-resolution reference data set (42). Spearman rank coefficients (ρ) describe the correlation between the sampled transcriptomes and the reference data set. The time points with the highest correlation coefficient are indicated. **(D)** Principal component analysis (PCA) of RNA-Seq data by condition and time point (TP). The outlier at TP3 (highlighted by an arrow) was removed from the analysis. **(E)** PCA of RNA-Seq data by condition and time point without the TP3 outlier mentioned in (D). Exclusion of this sample did not affect the overall pattern.

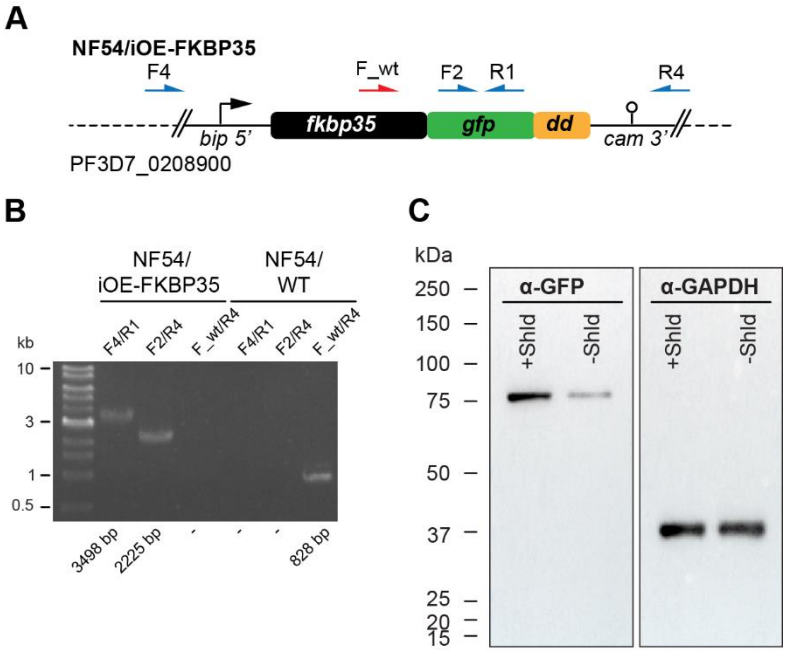

Figure S4. Characterization of NF54/iOE-FKBP35 parasites.

(A) Schematic of the modified *p230p* locus (PF3D7_0208900) in NF54/iOE-FKBP35 parasites, in which the overexpression cassette was introduced. This cassette consists of a *bip* promoter upstream of coding sequences of *fkbp35*, green fluorescent protein (*gfp*) and destabilization domain (*dd*), followed by the *cam 3'* region. Names and binding sites of the primers used for diagnostic PCRs are indicated. The primer F_wt only binds the unmodified *p230p* sequence. **(B)** Diagnostic PCRs performed on gDNA of NF54/iOE-FKBP35 parasites to confirm correct editing of the locus. PCRs performed on NF54/WT gDNA served as control. Numbers at the bottom indicate the expected band sizes. **(C)** Expression levels of the FKBP35-GFP-DD fusion protein were assessed by Western blot. Parasite cultures were split at 0-6 hpi and treated with Shield or the vehicle control EtOH. Protein lysates were collected 40 h later. α-GAPDH served as loading control. The expected size of the FKBP35-GFP-DD fusion protein is 74.2 kDa.

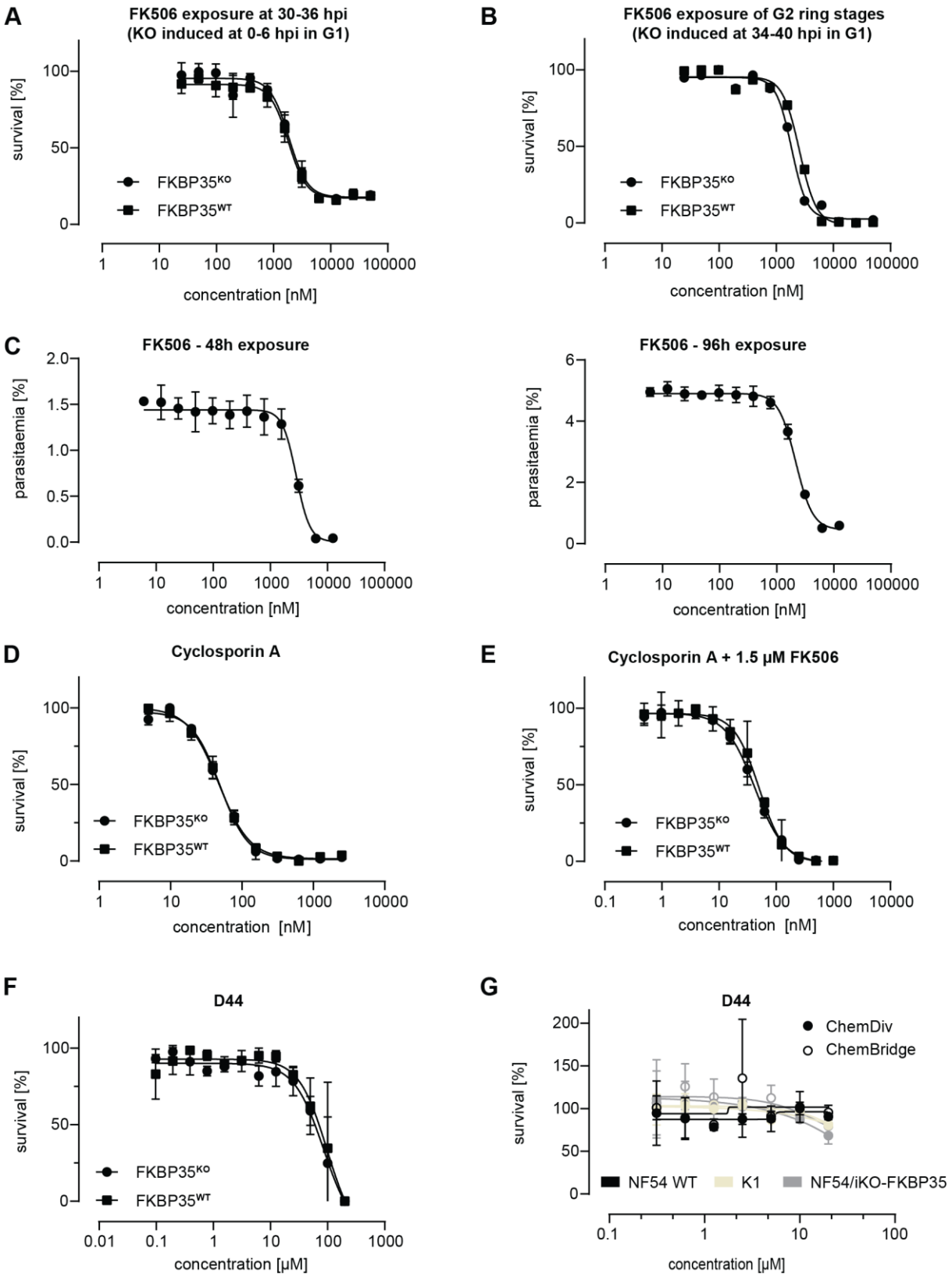

Figure S5. FKBP-targeting drugs fail at inhibiting parasite *Pf*FKBP35.

(A) Dose-response effect of FK506 on FKBP35^{KO} and FKBP35^{WT} parasites. The knockout was induced at 0-6 hpi and parasites were exposed to FK506 at 30-36 hpi. Survival rates were measured by flow cytometry in G2. n=3, error bars represent the standard error of the mean.

(B) Dose-response effect of FK506 on FKBP35$^{\mathbf{KO}}$ and FKBP35$^{\mathbf{WT}}$ parasites. The knockout was induced at 34-40 hpi in G1. Ring stage parasites of G2 were exposed to FK506 for 48 hours and survival rates were measured by flow cytometry in G3. Data points represent survival rates measured in a single experiment performed in technical duplicates. **(C)** Dose-response effect of FK506 on FKBP35$^{\mathbf{WT}}$ parasites over two IDCs. Parasites at 0-6 hpi were exposed to FK506 and incubated for 96 hours. Parasitaemia was measured by flow cytometry after 48 hours and 96 hours. Medium containing the appropriate drug concentrations was changed after 48 hours. n=3, error bars represent the standard error of the mean. **(D)** Dose-response effect of cyclosporin A on FKBP35$^{\mathbf{KO}}$ and FKBP35$^{\mathbf{WT}}$ parasites. Cylocsporin A, a known inhibitor of calcineurin when complexed with FKBP in other organisms (79), did not alter drug susceptibility between FKBP35$^{\mathbf{KO}}$ and FKBP35$^{\mathbf{WT}}$ parasites, suggesting that *Pf*FKBP35 is not involved in regulating calcineurin activity. The knockout was induced at 0-6 hpi. Parasites were exposed to cyclosporin A for 48 hours. n=3, error bars represent the standard error of the mean. **(E)** Dose-response effect of cyclosporin A in combination with a constant FK506 concentration on FKBP35$^{\mathbf{KO}}$ and FKBP35$^{\mathbf{WT}}$ parasites. The knockout was induced at 0-6 hpi. Parasites were subsequently exposed to cyclosporin A and 1.5 µM FK506 for 48 h. n=3, error bars represent the standard error of the mean. **(F)** Dose-response effect of D44 on FKBP35^{KO} and FKBP35$^{\mathbf{WT}}$. The knockout was induced at 0-6 hpi and parasites were exposed to D44 for 48 hours thereafter. Survival rates were determined using flow cytometry. n=3, error bars represent the standard error of the mean. **(G)** Dose-response effect of D44 on NF54 WT, K1 and NF54/iKO-FKBP35 parasites after 72 h exposure. Survival rates were determined using a hypoxanthine incorporation assay. Data points represent the mean of two technical replicates. Error bars represent the standard error of the mean.

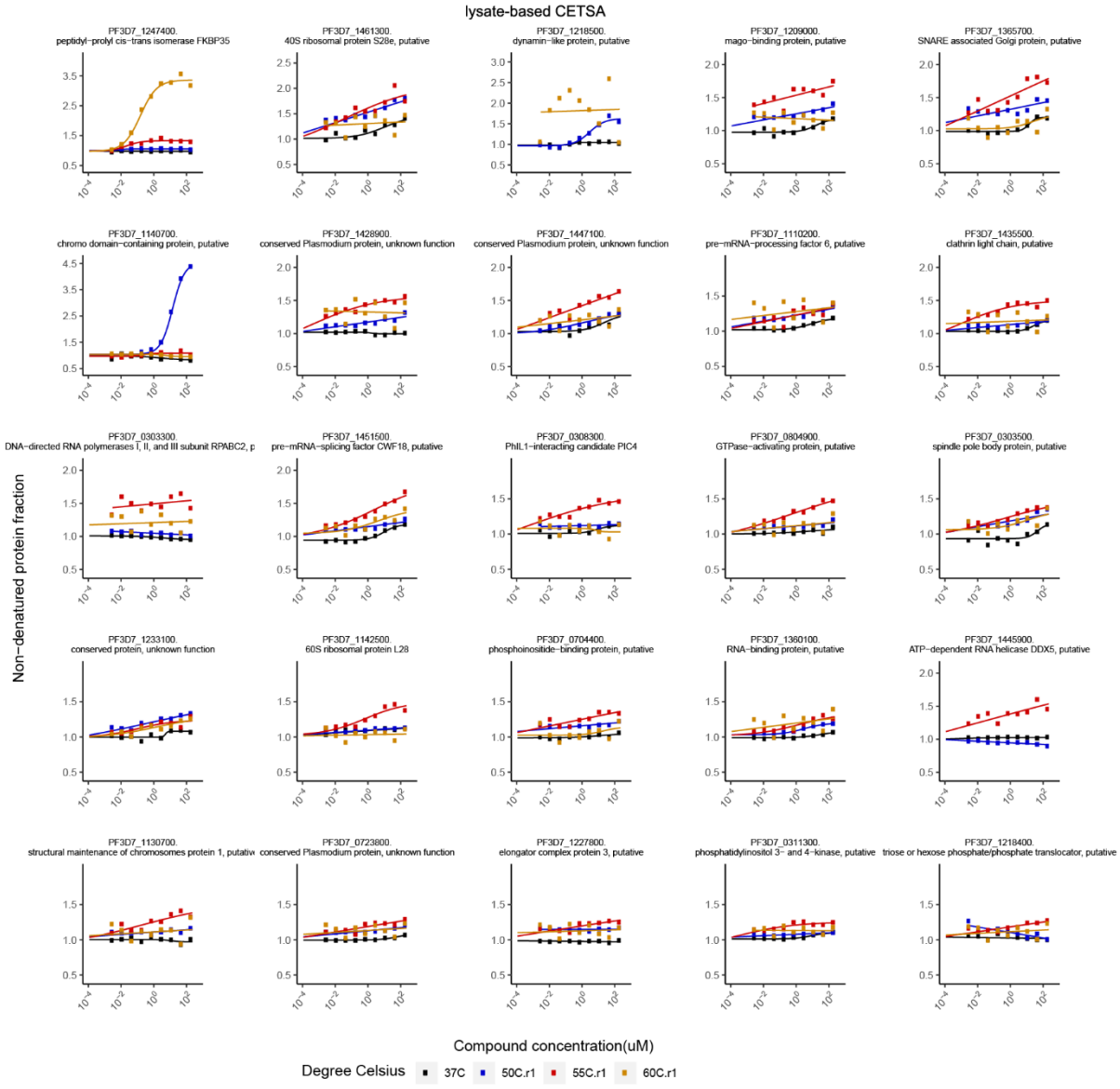

Figure S6. Putative FK506 interaction partners identified by protein lysate-based CETSA.

Proteins with an area under the curve (ΔAUC in protein lysate-based CETSA) greater than two median absolute deviations and an R^2 greater than 0.8 are listed. Bullets represent the abundance of non-denatured proteins in response to increasing FK506 concentrations under thermal challenge relative to a DMSO control. Colors indicate the temperatures used for protein denaturation; the black curve represents the non-denaturing control.

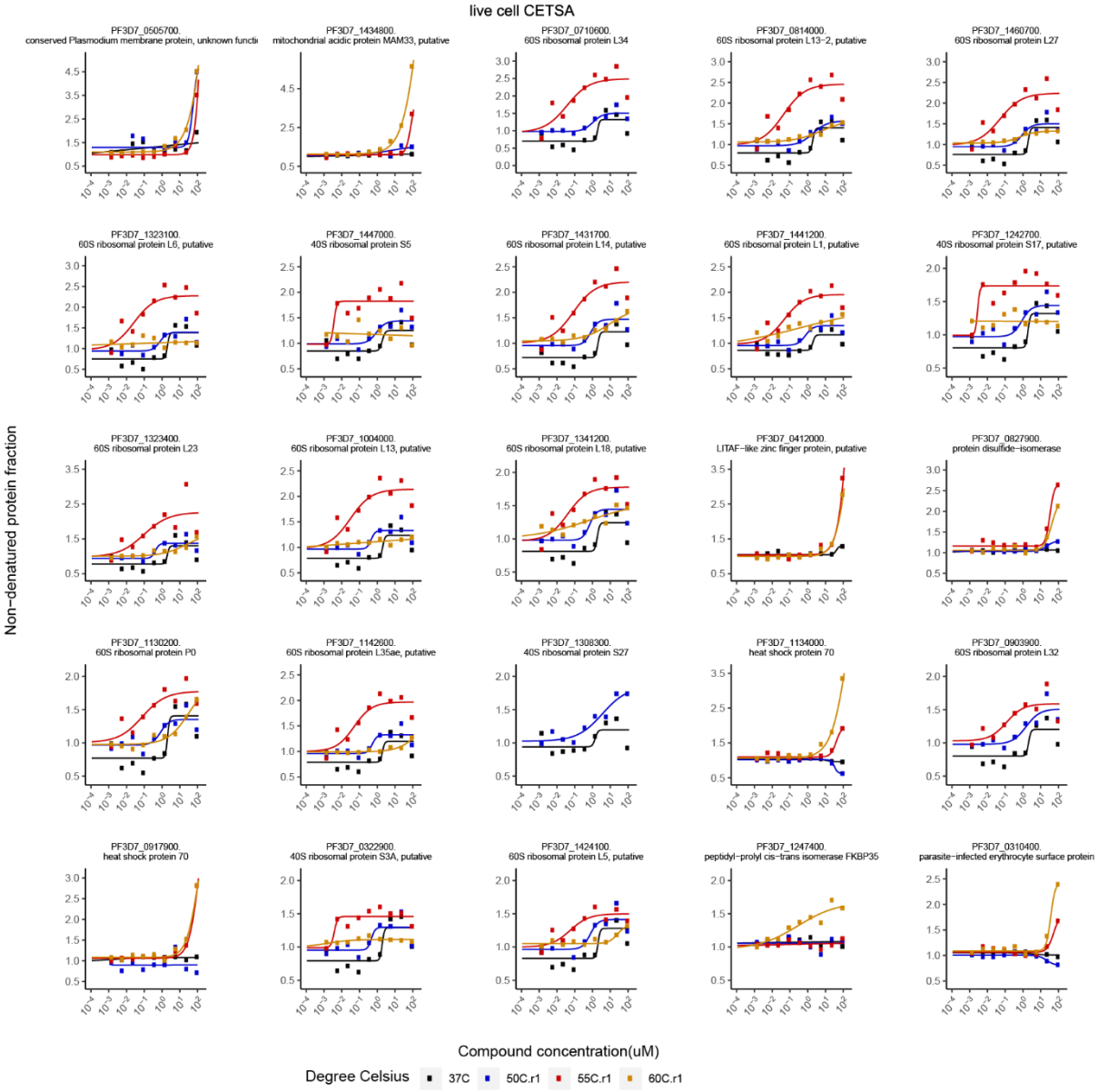

Figure S7. Putative FK506 interaction partners identified by live cell CETSA.

Proteins with an area under the curve (ΔAUC in live cell CETSA) greater than two median absolute deviations and an R^2 greater than 0.8 are listed. Bullets represent the abundance of non-denatured proteins in response to increasing FK506 concentrations under thermal challenge relative to a DMSO control. Colors indicate the temperatures used for heat challenge; the black curve represents the non-denaturing control.

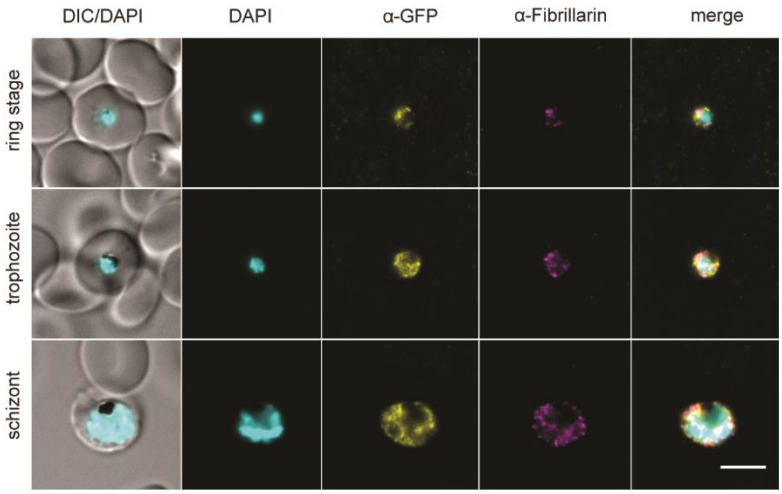

Figure S8. *Pf*FKBP35 localizes near fibrillarin-dense nuclear regions.

Localization of *Pf*FKBP35 (GFP) and fibrillarin in NF54/iKD-FKBP35 parasites at the ring, trophozoite and schizont stage assessed by immunofluorescence. DNA was stained with DAPI. Representative images are shown. Scale bar: 5 µm. DIC, differential interference contrast.

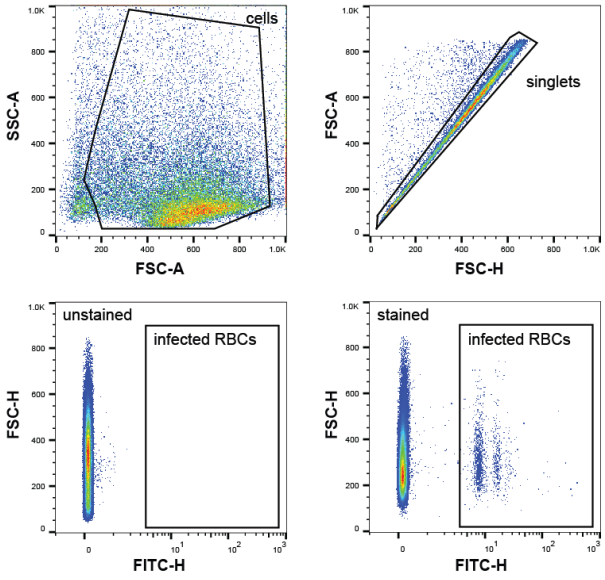

Figure S9. Gating strategy of flow cytometry data.

Representative flow cytometry plots of formaldehyde/glutaraldehyde-fixed parasite cultures are shown. The first plot shows the gate to distinguish cells from small debris (SSC-A vs. FSC-A). The ‘singlets’ gate (FSC-A vs. FSC-H) removes events with more than one cells. SYBR Green fluorescence intensity is used to identify parasite-infected RBCs (FSC-H vs. FITC-H). SSC, side scatter. FSC, forward scatter. FITC, fluorescein-5-isothiocyanate. A, area. H, height.

Table S1. Mass spectrometry data comparing the proteomes of FKBP35^{KO} and FKBP35^{WT} parasites.

Table S2. RNA-seq data comparing the transcriptomes of FKBP35^{KO} and FKBP35^{WT} parasites.

Table S3. CETSA data showing the relative abundance of soluble proteins under non-denaturing and denaturing conditions in response to increasing FK506 concentrations.

Table S4. Oligonucleotides used in this study.

5 References

1. WHO. World malaria report 2022. Geneva: WHO; 2022.

2. Ippolito MM, Moser KA, Kabuya JB, Cunningham C, Juliano JJ. Antimalarial Drug Resistance and Implications for the WHO Global Technical Strategy. Curr Epidemiol Rep. 2021;8(2):46-62.

3. Bell A, Wernli B, Franklin RM. Roles of peptidyl-prolyl cis-trans isomerase and calcineurin in the mechanisms of antimalarial action of cyclosporin A, FK506, and rapamycin. Biochem Pharmacol. 1994;48(3):495-503.

4. Bharatham N, Chang MW, Yoon HS. Targeting FK506 binding proteins to fight malarial and bacterial infections: current advances and future perspectives. Curr Med Chem. 2011;18(12):1874-89.

5. Monaghan P, Bell A. A Plasmodium falciparum FK506-binding protein (FKBP) with peptidyl-prolyl cis-trans isomerase and chaperone activities. Mol Biochem Parasitol. 2005;139(2):185-95.

6. Bell A, Monaghan P, Page AP. Peptidyl-prolyl cis-trans isomerases (immunophilins) and their roles in parasite biochemistry, host-parasite interaction and antiparasitic drug action. Int J Parasitol. 2006;36(3):261-76.

7. Kolos JM, Voll AM, Bauder M, Hausch F. FKBP Ligands-Where We Are and Where to Go? Front Pharmacol. 2018;9:1425.

8. Kang CB, Hong Y, Dhe-Paganon S, Yoon HS. FKBP family proteins: immunophilins with versatile biological functions. Neurosignals. 2008;16(4):318-25.

9. Bose S, Weikl T, Bügl H, Buchner J. Chaperone function of Hsp90-associated proteins. Science. 1996;274(5293):1715-7.

10. Furutani M, Ideno A, Iida T, Maruyama T. FK506 binding protein from a thermophilic archaeon, methanococcus thermolithotrophicus, has chaperone-like activity in vitro. Biochemistry. 2000;39(10):2822.

11. Yang WM, Yao YL, Seto E. The FK506-binding protein 25 functionally associates with histone deacetylases and with transcription factor YY1. Embo j. 2001;20(17):4814-25.

12. Kasahara K, Nakayama R, Shiwa Y, Kanesaki Y, Ishige T, Yoshikawa H, et al. Fpr1, a primary target of rapamycin, functions as a transcription factor for ribosomal protein genes cooperatively with Hmo1 in Saccharomyces cerevisiae. PLoS Genet. 2020;16(6):e1008865.

13. Cardenas ME, Zhu D, Heitman J. Molecular mechanisms of immunosuppression by cyclosporine, FK506, and rapamycin. Curr Opin Nephrol Hypertens. 1995;4(6):472-7.

14. Leneghan D, Bell A. Immunophilin-protein interactions in Plasmodium falciparum. Parasitology. 2015;142(11):1404-14.

15. Yoon HR, Kang CB, Chia J, Tang K, Yoon HS. Expression, purification, and molecular characterization of Plasmodium falciparum FK506-binding protein 35 (PfFKBP35). Protein Expr Purif. 2007;53(1):179-85.

16. Kumar R, Adams B, Musiyenko A, Shulyayeva O, Barik S. The FK506-binding protein of the malaria parasite, Plasmodium falciparum, is a FK506-sensitive chaperone with FK506-independent calcineurin-inhibitory activity. Mol Biochem Parasitol. 2005;141(2):163-73.

17. Alag R, Bharatham N, Dong A, Hills T, Harikishore A, Widjaja AA, et al. Crystallographic structure of the tetratricopeptide repeat domain of Plasmodium falciparum FKBP35 and its molecular interaction with Hsp90 C-terminal pentapeptide. Protein Sci. 2009;18(10):2115-24.

18. Zhang M, Wang C, Otto TD, Oberstaller J, Liao X, Adapa SR, et al. Uncovering the essential genes of the human malaria parasite Plasmodium falciparum by saturation mutagenesis. Science. 2018;360(6388).

19. Alag R, Qureshi IA, Bharatham N, Shin J, Lescar J, Yoon HS. NMR and crystallographic structures of the FK506 binding domain of human malarial parasite Plasmodium vivax FKBP35. Protein Sci. 2010;19(8):1577-86.

20. Goh CKW, Silvester J, Wan Mahadi WNS, Chin LP, Ying LT, Leow TC, et al. Expression and characterization of functional domains of FK506-binding protein 35 from Plasmodium knowlesi. Protein Eng Des Sel. 2018;31(12):489-98.

21. Bianchin A, Allemand F, Bell A, Chubb AJ, Guichou JF. Two crystal structures of the FK506-binding domain of Plasmodium falciparum FKBP35 in complex with rapamycin at high resolution. Acta Crystallogr D Biol Crystallogr. 2015;71(Pt 6):1319-27.

22. Kotaka M, Ye H, Alag R, Hu G, Bozdech Z, Preiser PR, et al. Crystal structure of the FK506 binding domain of Plasmodium falciparum FKBP35 in complex with FK506. Biochemistry. 2008;47(22):5951-61.

23. MacDonald CA, Boyd RJ. Computational insights into the suicide inhibition of Plasmodium falciparum Fk506-binding protein 35. Bioorg Med Chem Lett. 2015;25(16):3221-5.

24. Harikishore A, Niang M, Rajan S, Preiser PR, Yoon HS. Small molecule Plasmodium FKBP35 inhibitor as a potential antimalaria agent. Sci Rep. 2013;3:2501.

25. Harikishore A, Leow ML, Niang M, Rajan S, Pasunooti KK, Preiser PR, et al. Adamantyl derivative as a potent inhibitor of Plasmodium FK506 binding protein 35. ACS Med Chem Lett. 2013;4(11):1097-101.

26. Rajan S, Yoon HS. Structural insights into Plasmodium PPIases. Front Cell Infect Microbiol. 2022;12:931635.

27. MacDonald CA, Boyd RJ. Molecular docking study of macrocycles as Fk506-binding protein inhibitors. J Mol Graph Model. 2015;59:117-22.

28. Deepa P, Thirumeignanam D. Understanding the potency of malarial ligand (D44) in plasmodium FKBP35 and modelled halogen atom (Br, Cl, F) functional groups. J Mol Graph Model. 2020;97:107553.

29. Atack TC, Raymond DD, Blomquist CA, Pasaje CF, McCarren PR, Moroco J, et al. Targeted Covalent Inhibition of Plasmodium FK506 Binding Protein 35. ACS Med Chem Lett. 2020;11(11):2131-8.

30. Armstrong CM, Goldberg DE. An FKBP destabilization domain modulates protein levels in Plasmodium falciparum. Nat Methods. 2007;4(12):1007-9.

31. Banaszynski LA, Chen LC, Maynard-Smith LA, Ooi AG, Wandless TJ. A rapid, reversible, and tunable method to regulate protein function in living cells using synthetic small molecules. Cell. 2006;126(5):995-1004.

32. Collins CR, Das S, Wong EH, Andenmatten N, Stallmach R, Hackett F, et al. Robust inducible Cre recombinase activity in the human malaria parasite Plasmodium falciparum enables efficient gene deletion within a single asexual erythrocytic growth cycle. Mol Microbiol. 2013;88(4):687-701.

33. Jones ML, Das S, Belda H, Collins CR, Blackman MJ, Treeck M. A versatile strategy for rapid conditional genome engineering using loxP sites in a small synthetic intron in Plasmodium falciparum. Sci Rep. 2016;6:21800.

34. Kucharski M, Tripathi J, Nayak S, Zhu L, Wirjanata G, van der Pluijm RW, et al. A comprehensive RNA handling and transcriptomics guide for high-throughput processing of Plasmodium blood-stage samples. Malar J. 2020;19(1):363.

35. Wiley JD, Merino EF, Krai PM, McLean KJ, Tripathi AK, Vega-Rodríguez J, et al. Isoprenoid precursor biosynthesis is the essential metabolic role of the apicoplast during gametocytogenesis in Plasmodium falciparum. Eukaryot Cell. 2015;14(2):128-39.

36. Kennedy K, Cobbold SA, Hanssen E, Birnbaum J, Spillman NJ, McHugh E, et al. Delayed death in the malaria parasite Plasmodium falciparum is caused by disruption of prenylation-dependent intracellular trafficking. PLoS Biol. 2019;17(7):e3000376.

37. Mi H, Ebert D, Muruganujan A, Mills C, Albou LP, Mushayamaha T, et al. PANTHER version 16: a revised family classification, tree-based classification tool, enhancer regions and extensive API. Nucleic Acids Res. 2021;49(D1):D394-d403.

38. Boisvert FM, van Koningsbruggen S, Navascués J, Lamond AI. The multifunctional nucleolus. Nat Rev Mol Cell Biol. 2007;8(7):574-85.

39. Nissan TA, Bassler J, Petfalski E, Tollervey D, Hurt E. 60S pre-ribosome formation viewed from assembly in the nucleolus until export to the cytoplasm. Embo j. 2002;21(20):5539-47.

40. Plouffe D, Brinker A, McNamara C, Henson K, Kato N, Kuhen K, et al. In silico activity profiling reveals the mechanism of action of antimalarials discovered in a high-throughput screen. Proc Natl Acad Sci U S A. 2008;105(26):9059-64.

41. Schmidt EK, Clavarino G, Ceppi M, Pierre P. SUnSET, a nonradioactive method to monitor protein synthesis. Nat Methods. 2009;6(4):275-7.

42. Bozdech Z, Llinás M, Pulliam BL, Wong ED, Zhu J, DeRisi JL. The transcriptome of the intraerythrocytic developmental cycle of Plasmodium falciparum. PLoS Biol. 2003;1(1):E5.

43. Barnum KJ, O'Connell MJ. Cell cycle regulation by checkpoints. Methods Mol Biol. 2014;1170:29-40.

44. Monaghan P, Leneghan DB, Shaw W, Bell A. The antimalarial action of FK506 and rapamycin: evidence for a direct effect on FK506-binding protein PfFKBP35. Parasitology. 2017;144(7):869-76.

45. Van Duyne GD, Standaert RF, Karplus PA, Schreiber SL, Clardy J. Atomic structure of FKBP-FK506, an immunophilin-immunosuppressant complex. Science. 1991;252(5007):839-42.

46. Dziekan JM, Yu H, Chen D, Dai L, Wirjanata G, Larsson A, et al. Identifying purine nucleoside phosphorylase as the target of quinine using cellular thermal shift assay. Sci Transl Med. 2019;11(473).

47. Dziekan JM, Wirjanata G, Dai L, Go KD, Yu H, Lim YT, et al. Cellular thermal shift assay for the identification of drug-target interactions in the Plasmodium falciparum proteome. Nat Protoc. 2020;15(6):1881-921.

48. Tan CSH, Go KD, Bisteau X, Dai L, Yong CH, Prabhu N, et al. Thermal proximity coaggregation for system-wide profiling of protein complex dynamics in cells. Science. 2018;359(6380):1170-7.

49. Paul AS, Saha S, Engelberg K, Jiang RH, Coleman BI, Kosber AL, et al. Parasite Calcineurin Regulates Host Cell Recognition and Attachment by Apicomplexans. Cell Host Microbe. 2015;18(1):49-60.

50. Desjardins RE, Canfield CJ, Haynes JD, Chulay JD. Quantitative assessment of antimalarial activity in vitro by a semiautomated microdilution technique. Antimicrob Agents Chemother. 1979;16(6):710-8.

51. Ünal CM, Steinert M. FKBPs in bacterial infections. Biochim Biophys Acta. 2015;1850(10):2096-102.

52. Gudavicius G, Dilworth D, Serpa JJ, Sessler N, Petrotchenko EV, Borchers CH, et al. The prolyl isomerase, FKBP25, interacts with RNA-engaged nucleolin and the pre-60S ribosomal subunit. Rna. 2014;20(7):1014-22.

53. Sydorskyy Y, Dilworth DJ, Halloran B, Yi EC, Makhnevych T, Wozniak RW, et al. Nop53p is a novel nucleolar 60S ribosomal subunit biogenesis protein. Biochem J. 2005;388(Pt 3):819-26.

54. Ferbitz L, Maier T, Patzelt H, Bukau B, Deuerling E, Ban N. Trigger factor in complex with the ribosome forms a molecular cradle for nascent proteins. Nature. 2004;431(7008):590-6.

55. Callebaut I, Mornon JP. Trigger factor, one of the Escherichia coli chaperone proteins, is an original member of the FKBP family. FEBS Lett. 1995;374(2):211-5.

56. Rodriguez-Corona U, Sobol M, Rodriguez-Zapata LC, Hozak P, Castano E. Fibrillarin from Archaea to human. Biol Cell. 2015;107(6):159-74.

57. Thiry M, Lafontaine DL. Birth of a nucleolus: the evolution of nucleolar compartments. Trends in cell biology. 2005;15(4):194-9.

58. Lambros C, Vanderberg JP. Synchronization of Plasmodium falciparum erythrocytic stages in culture. J Parasitol. 1979;65(3):418-20.

59. Trager W, Jenson JB. Cultivation of malarial parasites. Nature. 1978;273(5664):621-2.

60. Brancucci NMB, Gerdt JP, Wang C, De Niz M, Philip N, Adapa SR, et al. Lysophosphatidylcholine Regulates Sexual Stage Differentiation in the Human Malaria Parasite Plasmodium falciparum. Cell. 2017;171(7):1532-44.e15.

61. Filarsky M, Fraschka SA, Niederwieser I, Brancucci NMB, Carrington E, Carrió E, et al. GDV1 induces sexual commitment of malaria parasites by antagonizing HP1-dependent gene silencing. Science. 2018;359(6381):1259-63.

62. Knuepfer E, Napiorkowska M, van Ooij C, Holder AA. Generating conditional gene knockouts in Plasmodium - a toolkit to produce stable DiCre recombinase-expressing parasite lines using CRISPR/Cas9. Sci Rep. 2017;7(1):3881.

63. Gibson DG, Young L, Chuang RY, Venter JC, Hutchison CA, 3rd, Smith HO. Enzymatic assembly of DNA molecules up to several hundred kilobases. Nat Methods. 2009;6(5):343-5.

64. Ashdown GW, Dimon M, Fan M, Sánchez-Román Terán F, Witmer K, Gaboriau DCA, et al. A machine learning approach to define antimalarial drug action from heterogeneous cell-based screens. Sci Adv. 2020;6(39).

65. Tibúrcio M, Yang ASP, Yahata K, Suárez-Cortés P, Belda H, Baumgarten S, et al. A Novel Tool for the Generation of Conditional Knockouts To Study Gene Function across the Plasmodium falciparum Life Cycle. mBio. 2019;10(5).

66. Thommen BT, Passecker A, Buser T, Hitz E, Voss TS, Brancucci NMB. Revisiting the Effect of Pharmaceuticals on Transmission Stage Formation in the Malaria Parasite Plasmodium falciparum. Front Cell Infect Microbiol. 2022;12:802341.

67. Thomas JA, Collins CR, Das S, Hackett F, Graindorge A, Bell D, et al. Development and Application of a Simple Plaque Assay for the Human Malaria Parasite Plasmodium falciparum. PLoS One. 2016;11(6):e0157873.

68. Daubenberger CA, Tisdale EJ, Curcic M, Diaz D, Silvie O, Mazier D, et al. The N'-terminal domain of glyceraldehyde-3-phosphate dehydrogenase of the apicomplexan Plasmodium falciparum mediates GTPase Rab2-dependent recruitment to membranes. Biol Chem. 2003;384(8):1227-37.

69. Ahrné E, Glatter T, Viganò C, Schubert C, Nigg EA, Schmidt A. Evaluation and Improvement of Quantification Accuracy in Isobaric Mass Tag-Based Protein Quantification Experiments. J Proteome Res. 2016;15(8):2537-47.

70. Ritchie ME, Phipson B, Wu D, Hu Y, Law CW, Shi W, et al. limma powers differential expression analyses for RNA-sequencing and microarray studies. Nucleic Acids Res. 2015;43(7):e47.

71. McLean KJ, Jacobs-Lorena M. Plasmodium falciparum Maf1 Confers Survival upon Amino Acid Starvation. mBio. 2017;8(2).

72. Kim D, Paggi JM, Park C, Bennett C, Salzberg SL. Graph-based genome alignment and genotyping with HISAT2 and HISAT-genotype. Nat Biotechnol. 2019;37(8):907-15.

73. Aurrecoechea C, Brestelli J, Brunk BP, Dommer J, Fischer S, Gajria B, et al. PlasmoDB: a functional genomic database for malaria parasites. Nucleic Acids Res. 2009;37(Database issue):D539-43.

74. Love MI, Huber W, Anders S. Moderated estimation of fold change and dispersion for RNA-seq data with DESeq2. Genome Biol. 2014;15(12):550.

75. Blighe K, Rana S, Lewis M. EnhancedVolcano: Publication-ready volcano plots with enhanced colouring and labeling. R package version 1.16.0. https://githubcom/kevinblighe/EnhancedVolcano. 2022.

76. Kassambara A. ggcorrplot: Visualization of a Correlation Matrix using 'ggplot2'. R package version 0.1.3, . https://CRANR-projectorg/package=ggcorrplot. 2022.

77. Yeh E, DeRisi JL. Chemical rescue of malaria parasites lacking an apicoplast defines organelle function in blood-stage Plasmodium falciparum. PLoS Biol. 2011;9(8):e1001138.

78. Lu KY, Pasaje CFA, Srivastava T, Loiselle DR, Niles JC, Derbyshire E. Phosphatidylinositol 3-phosphate and Hsp70 protect Plasmodium falciparum from heat-induced cell death. Elife. 2020;9.

79. Dumont FJ. FK506, an immunosuppressant targeting calcineurin function. Curr Med Chem. 2000;7(7):731-48.